



1 On the understanding of tropospheric fast photochemistry: airborne 2 observations of peroxy radicals during the EMeRGe-Europe campaign

3 Midhun George¹, Maria Dolores Andrés Hernández¹, Vladyslav Nenakhov^{1*}, Yangzhuoran Liu¹, John
4 Philip Burrows¹; Birger Bohn²; Eric Förster³, Florian Obersteiner³, Andreas Zahn³; Theresa Harlaß⁴,
5 Helmut Ziereis⁴, Hans Schlager⁴; Benjamin Schreiner⁵, Flora Kluge⁵, Katja Bigge⁵, and Klaus Pfeilsticker⁵

6 ¹ Institute of Environmental Physics, University of Bremen, Germany

7 ² Institute of Energy and Climate Research, IEK-8: Troposphere, Forschungszentrum Jülich GmbH, Jülich, Germany

8 ³ Institute of Meteorology and Climate Research, Karlsruhe Institute of Technology, Karlsruhe, Germany

9 ⁴ Deutsches Zentrum für Luft- und Raumfahrt (DLR), Institut für Physik der Atmosphäre, Oberpfaffenhofen, Germany

10 ⁵ Institute of Environmental Physics, University of Heidelberg, Heidelberg, Germany

11 * now at Flight Experiments, DLR Oberpfaffenhofen, Germany

12 Correspondence to M. George (midhun@iup.physik.uni-bremen.de) and M. D. Andrés Hernández (lola@iup.physik.uni-bremen.de).
13

14 **Abstract.** In this study, airborne measurements of the sum of hydroperoxyl (HO₂) and organic peroxy (RO₂) radicals that react
15 with NO to produce NO₂, i.e. RO₂^{*}, coupled with actinometry and other key trace gases measurements, have been used to test the
16 current understanding of the fast photochemistry in the outflow of major population centres (MPCs). All measurements were
17 made during the airborne campaign of the EMeRGe (Effect of Megacities on the transport and transformation of pollutants on
18 the Regional to Global scales) project in Europe on-board the High Altitude Long range research aircraft (HALO). The on-board
19 measurements of RO₂^{*} were made using the in-situ instrument Peroxy Radical Chemical Enhancement and Absorption
20 Spectrometer (PeRCEAS). RO₂^{*} mixing ratios up to 120 pptv were observed in air masses of different origins and composition
21 under different local actinometrical conditions during seven HALO research flights in July 2017 over Europe.

22 The range and variability of the RO₂^{*} measurements agree reasonably well with radical production rates estimated using
23 photolysis frequencies and RO₂^{*} precursor concentrations measured on-board. RO₂^{*} is primarily produced following the
24 photolysis of ozone (O₃), formaldehyde (HCHO), glyoxal (CHOCHO), and nitrous acid (HONO) in the airmasses investigated.
25 The suitability of photostationary steady-state (PSS) assumptions to estimate the mixing ratios and the variability of RO₂^{*} during
26 the airborne observations is investigated. The PSS assumption is robust enough to calculate RO₂^{*} mixing ratios for most
27 conditions encountered in air masses measured. The similarities and discrepancies between measured and calculated RO₂^{*}
28 mixing ratios are analysed stepwise. The parameters, which predominantly control the RO₂^{*} mixing ratios under different
29 chemical and physical regimes, are identified during the analysis. The dominant removal processes of RO₂^{*} in the airmasses
30 measured up to 2000 m are the loss of OH and RO through the reaction with NO_x during the radical interconversion. Above 2000
31 m, HO₂ – HO₂ and HO₂ – RO₂ reactions dominate RO₂^{*} loss reactions. RO₂^{*} calculations underestimated (< 20 %) the
32 measurements by the analytical expression inside the pollution plumes probed. The underestimation is attributed to the
33 limitations of the PSS analysis to take into account the production of RO₂^{*} through oxidation and photolysis of the OVOCs not
34 measured during EMeRGe.

35 1. Introduction

36 Hydroperoxyl (HO₂) and organic peroxy (RO₂, where R stands for any organic group) radicals are reactive species that play a
37 key role in the chemistry of the troposphere. In combination with the hydroxyl (OH) radical, HO₂ and RO₂ take part in rapid

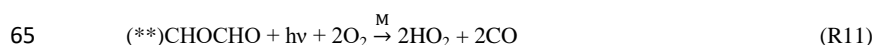
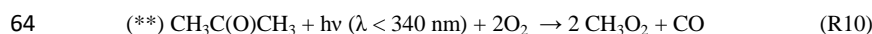
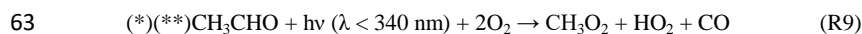
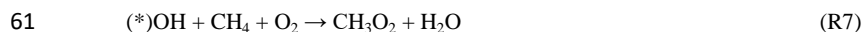
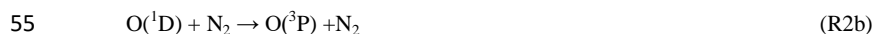
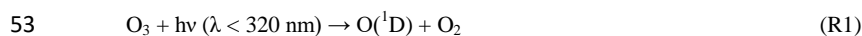


38 chemical processes that control the lifetime of many key trace constituents in the troposphere. Examples of key tropospheric
39 processes involving HO₂ and RO₂ are as follows:

- 40 • the catalytic cycles, which produce and destroy ozone (O₃)
- 41 • the generation of key inorganic acids, which are precursors of aerosol (e.g. sulphuric acid, H₂SO₄) and important
42 chemical constituents (e.g. nitric acid, HNO₃) in both summer and winter smog
- 43 • the generation of organic acids; the production of hygroscopic hydrogen peroxide (H₂O₂) and organic peroxides
44 (ROOH), which enter aerosol and cloud droplets
- 45 • the generation of organic peroxy nitrates (RO₂NO₂), peroxyacetyl nitrate (CH₃COO₂NO₂, PAN) and other summer
46 smog constituents.

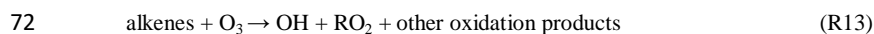
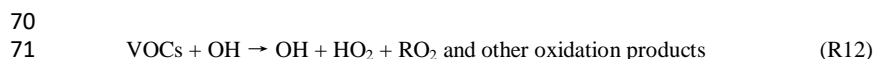
47 The abundance of HO₂ and RO₂ in the free troposphere has a non-linear and complex dependency on photochemistry, initiated
48 by solar actinic radiation, and on the concentration of the precursors, such as carbon monoxide (CO), volatile organic compounds
49 (VOCs), and peroxides. It also strongly depends on the amounts of nitrogen monoxide (NO) and nitrogen dioxide (NO₂) due to
50 the gas-phase reactions of NO and NO₂ with the OH and organic oxy (RO) radicals formed during the radical interconversion.
51 The main production and loss processes of HO₂ and RO₂ in the troposphere are summarised as follows:

52 a) Production processes of HO₂ and RO₂ through photolysis and oxidation by OH formed through photolysis



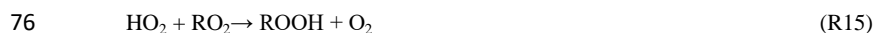
66 (*) The CH₃ produced from the oxidation of CH₄ or the photolysis of VOCs further reacts with O₂ to form CH₃O₂. The net reaction is written since the formation
67 of CH₃O₂ is much faster than the CH₃ formation due to the high amount of O₂ present in the atmosphere.

68 (***) H and CHO formed through the VOC photolysis further react with O₂ to form HO₂. The net reaction is written since the formation of HO₂ is much faster
69 than the H and CHO formation due to the high amount of O₂ present in the atmosphere.



73

74 b) Loss processes of HO_2 and RO_2

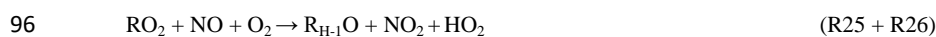


84 In addition, HO_2 and RO_2 undergo radical interconversion processes through the following reactions:



90 R23 is one of the most important reactions in the troposphere as it leads to O_3 formation through R27 and R28.

91 Provided that there is sufficient insolation to ensure rapid photochemical processing and all species involved are known, the sum
92 of HO_2 and RO_2 that react with NO to produce NO_2 can be estimated from a photochemical steady-state (PSS) assumption in
93 which production and loss mechanisms are equally important. The HO_2 + RO_2 concentrations and mixing ratios can be estimated
94 using the PSS assumption for NO_2 by considering the following reactions:





100 Assuming a PSS for NO_2 , this leads to Eq. 1

101
$$[HO_2 + RO_2]_{PSS} = \frac{k_{NO+O_3}}{k_{NO+(HO_2+RO_2)}} \left(\frac{j_{NO_2}[NO_2]}{k_{NO+O_3}[NO]} - [O_3] \right)$$
 (Eq.1)

102 where j_{NO_2} is the photolysis frequency of NO_2 ; k_{NO+O_3} (1.9×10^{-14} cm³ molecules⁻¹ s⁻¹) is the rate coefficient of the reaction of
103 NO with O_3 and $k_{NO+(HO_2+RO_2)}$ is the weighted average rate coefficient assumed for the reactions of peroxy radicals with NO.

104 The comparison of $[HO_2 + RO_2]_{PSS}$ calculated using Eq.1 with ground-based (e.g. Ridley et al., 1992; Cantrell et al., 1997;
105 Carpenter et al., 1998; Volz-Thomas et al., 2003), and airborne measurements, has shown in the past different degree of
106 agreement. The underestimations and overestimations found in air masses with different chemical compositions are not well
107 understood. In the case of airborne measurements, the PSS calculation generally overestimates that measured peroxy radicals
108 (Cantrell et al., 2003a, 2003b). The differences observed could not be attributed to systematic changes in NO, altitude, water
109 vapour and temperature, although these variables are often correlated.

110 Ground-based (Mihelcic et al., 2003; Kanaya et al., 2007, 2012; Elshorbany et al., 2012; Lu et al., 2012, 2013; Tan et al., 2017,
111 2018; Whalley et al., 2018, 2021; Lew et al., 2020) and airborne (Crawford et al., 1999; Tan et al., 2001; Cantrell et al., 2003b)
112 measurements have also been compared with model simulations of HO_2 and RO_2 . The discrepancies encountered depend upon
113 the chemical composition of the air mass and the chemical mechanisms and constraints used in the model simulations. Tan et al.,
114 2019 and Whalley et al., 2021 reported experimental radical budget calculations based on the published reaction rate coefficients
115 of fundamental reactions (R1 to R26) controlling OH, HO_2 and RO_2 in the lower troposphere and ground-based measurements of
116 all relevant reactants and photolysis frequencies. In this study, a similar approach has been used to calculate the amount of
117 peroxy radicals in the air masses measured on-board of the **H**igh **A**ltitude **L**ong range (HALO) research aircraft over Europe
118 during the first campaign of the EMeRGe (**E**ffect of **M**egacities on the transport and transformation of pollutants on the **R**egional
119 to **G**lobal scales) project. The available on-board measurements of RO_2^* are defined as the total sum of OH, RO and peroxy
120 radicals reacting with NO to produce NO_2 (i.e., $RO_2^* = OH + \sum RO + HO_2 + \sum RO_2$, where RO_2 are the organic peroxy radicals
121 reacting with NO to produce NO_2). Since the amount of OH and RO is much smaller, RO_2^* to a good approximation is the sum
122 of HO_2 and those RO_2 radicals that react with NO to produce NO_2 . For the calculation, RO_2^* is assumed to be in PSS, and an
123 analytical expression is developed with a manageable degree of complexity to estimate the concentration and mixing ratios of
124 RO_2^* . The simultaneous on-board measurements of trace gases and photolysis frequencies are used to constrain the estimate of
125 the RO_2^* concentration.

126 In contrast to other experimental deployments, the concentrations and/or mixing ratios of the majority of the key species
127 involved in reactions R1 to R26 were continuously measured on-board HALO during the EMeRGe campaign. This minimises
128 the number of assumptions required for the calculations of RO_2^* . Consequently, this data set provides an excellent opportunity to
129 gain a deeper insight into the source and sink reactions of RO_2^* and the applicability of the PSS assumption for the different
130 pollution regimes and related weather conditions in the free troposphere.

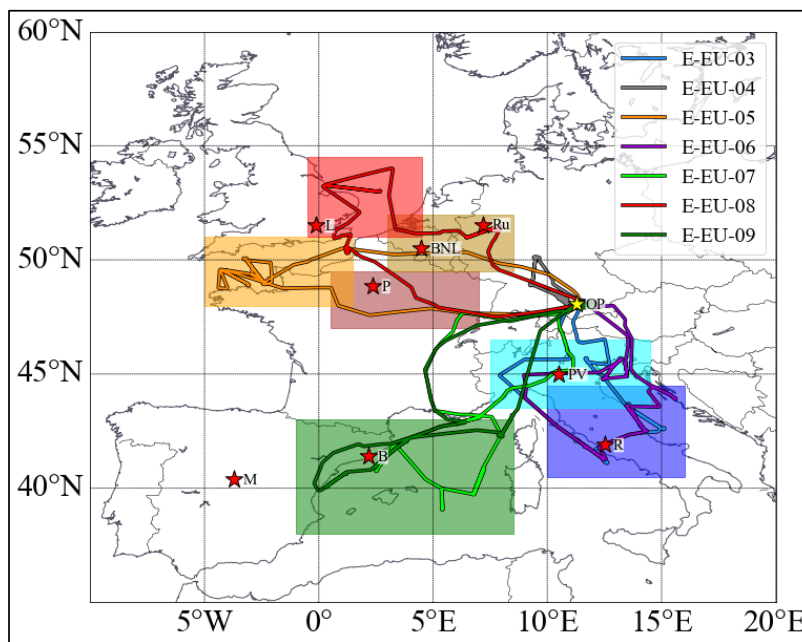
131



132 2. EMeRGe field campaign in Europe

133 The overarching objective of the EMeRGe project is to test and improve the current understanding of the photochemical and
134 heterogeneous processing of pollution outflows from major population centres (MPCs) and their impact on the atmosphere. Two
135 intensive observational periods (IOP) were carried out to investigate selected European and Asian MPC outflows. The European
136 IOP took place from 10 to 28 July 2017 (<http://www.iup.uni-bremen.de/emerge/home/home.html>). An extensive set of in-situ
137 and remote-sensing airborne measurements of trace gases and aerosol particles were made on-board the HALO aircraft (see
138 www.halo-spp.de) along flight tracks in the lower layers of the troposphere from northwest Europe to the Mediterranean region.

139 HALO carried out a total of 53 flight hours distributed over seven flights to investigate the chemical composition of the outflows
140 from the target MPCs: London, Paris, Benelux/ Ruhr metropolitan area, Po Valley, and urban agglomerations such as Rome,
141 Madrid, and Barcelona. The flight tracks are shown in Fig. 1. All HALO flights started from the HALO base at the DLR in
142 Oberpfaffenhofen, southwest of Munich, Germany. To achieve the scientific goals, 60 % of the flights were carried out below
143 3000 m. Vertical profiles of trace constituents were typically made in three stable flight levels upwind and downwind of the
144 target MPCs. The flights are named E-EU-FN, where E stands for EMeRGe, EU for Europe, and FN is the two-digit flight
145 number. More details about the EMeRGe IOP in Europe and the set of instruments deployed on-board the HALO aircraft are
146 described elsewhere (Andrés Hernández et al., 2021).



147
148 Figure 1: The research flight tracks made by HALO during the EMeRGe-Europe campaign on 11, 13, 17, 20, 24, 26 and 28 July
149 2017 (E-EU-03 to E-EU-09, respectively, colour coded). MPC target areas are colour coded by shading, and the targeted
150 locations/regions are marked with red stars, M: Madrid, B: Barcelona, P: Paris, L: London; BNL: BeNeLux; Ru: Ruhr area; PV:
151 Po Valley, R: Rome. The location of the HALO base at the DLR in Oberpfaffenhofen, Germany (OP) is indicated by a yellow
152 star.

153 3. PeRCEAS and other instruments on-board

154 The RO_2^* measurements on-board the HALO research aircraft during EMeRGe were made using the Peroxy Radical Chemical
155 Enhancement and Absorption Spectrometer (PeRCEAS). PeRCEAS combines the Peroxy Radical Chemical Amplification



156 (PerCA) and Cavity Ring-Down Spectroscopy (CRDS) techniques in a dual-channel instrument. Each channel has a separate
157 chemical reactor and detector, which operate alternatively in both background and amplification modes, i.e. without and with the
158 addition of CO, to account for the rapid background variations during airborne measurements. In the amplification mode, the
159 sum of the NO₂ produced from ambient RO₂^{*} through the chain reaction, the ambient NO₂, the NO₂ produced from the ambient
160 O₃ – NO reagent gas reaction and the NO₂ produced in the inlet from any other sources (e.g. thermal decomposition of PAN) is
161 measured. In the background mode, the sum of the ambient NO₂, the NO₂ produced from the ambient O₃ – NO reagent gas
162 reaction and NO₂ produced in the inlet from any other sources is measured. The RO₂^{*} is retrieved by dividing the difference in
163 NO₂ concentration (ΔNO_2) between amplification and background mode by the conversion efficiency of RO₂^{*} to NO₂, which is
164 referred to as eCL (effective chain length). The PerCEAS instrument and its specifications have been described in detail
165 elsewhere (Horstjann et al., 2014, George et al., 2020).

166 The two chemical reactors for sampling the ambient air are part of the **DU**al channel Airborne peroxy radical Chemical
167 Amplifier (DUALER) inlet installed inside a pylon located on the outside of the HALO fuselage. During the EMERGe campaign
168 in Europe, a reagent gas mixing ratio of 30 ppmv NO ([NO] = 1.46×10^{14} molecules cm⁻³ at 296 K) and of 9 % CO ([CO] = 4.4
169 $\times 10^{17}$ molecules cm⁻³ at 296 K) were added to the sample flow for the chemical conversion of RO₂^{*} to NO₂. The DUALER inlet
170 was operated at an internal pressure of 200 mbar to achieve stable chemical conversion. The average eCL under these operational
171 conditions was determined to be 50 ± 8 from laboratory calibrations, where the error is the standard deviation estimated from the
172 reproducibility of the experimental determinations. The HO₂ and RO₂ detection sensitivity depends on the reagent gas NO
173 concentration due to the rate coefficient of reaction R22 being larger than that for R19. For the measurement conditions used
174 during the IOP in Europe, the ratio $\alpha = \text{eCL}_{\text{CH}_3\text{O}_2} / \text{eCL}_{\text{HO}_2}$ is 65% (George et al., 2020).

175 Although the DUALER pressure is kept constant below the ambient pressure, variations in dynamical pressure > 10 mbar during
176 the flight can change the residence time and induce turbulences inside the inlet (Kartal et al., 2010; George et al., 2020). These
177 may lead to different physical losses of radicals before amplification and affect the eCL. In the measurements presented in this
178 study, variations in dynamical pressure of this magnitude were only encountered during flight level changes of the aircraft. When
179 used during the analysis, these data sets are either excluded or flagged (P_flag). The effect of the ambient air humidity on eCL
180 (Mihele and Hastie, 1998; Mihele et al., 1999; Reichert et al., 2003) has been accounted for by a calibration procedure reported
181 in George et al. (2020).

182 In addition to the measurement of RO₂^{*} from PerCEAS, other in-situ and remote-sensing measurements and basic aircraft data
183 from HALO are used in this study. Details of the corresponding instruments are summarised in Table 1. Concerning the data
184 obtained by the remote sensing instruments, the miniDOAS retrieves the Slant Column Density (SCD) of the target gas and a
185 scaling gas (O₄) towards the horizon at the flight altitude. From this, mixing ratios of the targeted gas within the line of sight is
186 estimated using RT modelling (Stutz et al., 2017; Hüneke et al., 2017; Kluge et al., 2020; Rotermund et al., 2021). The HAIDI
187 instrument retrieves SCDs below the aircraft. The SCDs from HAIDI are then converted to mixing ratios using the
188 corresponding geometric Air Mass Factor (AMF) under a well-mixed NO₂ layer assumption. As a result of this assumption, the
189 calculated mixing ratios for HAIDI target gases are lower limits and close to the actual values while flying within and close to a
190 well-mixed boundary layer. Despite the differences in sampling volume and temporal and spatial resolution in the in-situ and
191 remote sensing measurement techniques, the concentration of common and related species obtained are in reasonable agreement
192 (Schumann, 2020).

193



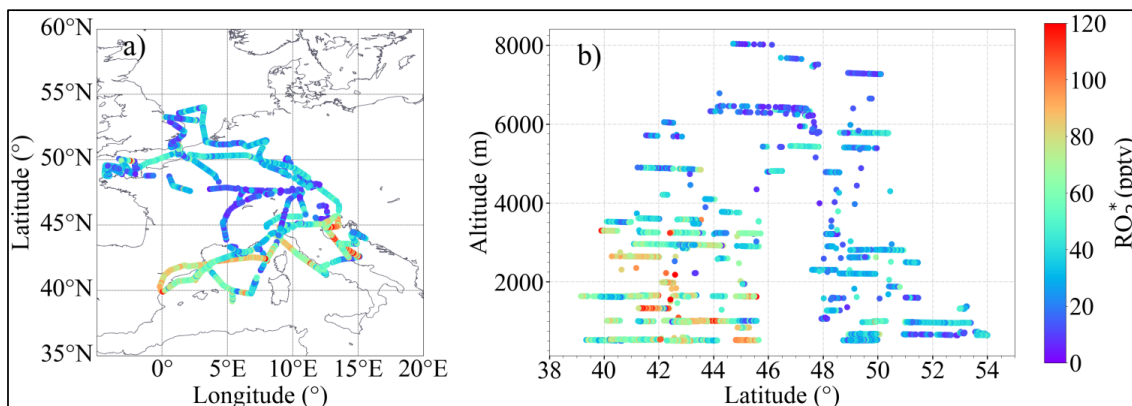
194 Table 1: List of the airborne measurements and instrumentation used in this study. PeRCA: Peroxy Radical Chemical Amplification;
 195 CRDS: Cavity Ring-Down Spectroscopy; PTR-MS: Proton-Transfer-Reaction Mass Spectrometer; AT-BS: Adsorption Tube and Bag air
 196 Sampler; TD-GC-MS: Thermal Desorption Gas Chromatography and Mass Spectrometry; DOAS: Differential Optical Absorption
 197 Spectrometry; Univ: University; KIT: Karlsruher Institut für Technologie; DLR: Deutsches Zentrum für Luft- und Raumfahrt; IPA: Institut für
 198 Physik der Atmosphäre; FZ: Forschungszentrum; FX: Flugexperimente.

Trace gas-in situ measurements				
Species/parameters	Acronym	Institution	Technique/Instrument	Reference
$\text{RO}_2^* = \text{HO}_2 + \sum \text{RO}_2$	PeRCEAS	Univ. Bremen	PeRCA + CRDS	George et al., 2020
OVOC	HKMS	KIT Karlsruhe	PTR-MS	Brito and Zahn, 2011
O_3	FAIRO	KIT Karlsruhe	UV-Photometry/ Chemiluminescence	Zahn et al., 2012
O_3, CO	AMTEX	DLR-IPA	UV-Photometry/ VUV-Fluorimetry	Gerbige et al., 1996
NO, NO_y	AENEAS	DLR-IPA	Chemiluminescence/ Gold converter	Ziereis et al., 2004
CO_2, CH_4	CATS	DLR-IPA	CRDS	Chen et al., 2010
Trace gas- remote sensing measurements				
Species/parameters	Acronym	Institution	Technique/Instrument	Reference
$\text{NO}_2, \text{HONO}, \text{CH}_2\text{O}, \text{C}_2\text{H}_2\text{O}_2, \text{C}_3\text{H}_4\text{O}_2$	miniDOAS	Univ. Heidelberg	DOAS / UV-nIR; 2D optical spectrometer	Hüneke et al., 2017
NO_2	HAIDI	Univ. Heidelberg	DOAS / 3x2D-imaging spectrometers	General et al., 2014
Other parameters				
Species/parameters	Acronym	Institution	Technique/Instrument	Reference
Spectral actinic flux density (up/down) Photolysis frequencies	HALO-SR	FZ Jülich	CCD spectro- radiometry	Bohn and Lohse, 2017
Basic aircraft data	BAHAMAS	DLR-FX	various	Mallaun et al., 2015

199 4. Results and discussion

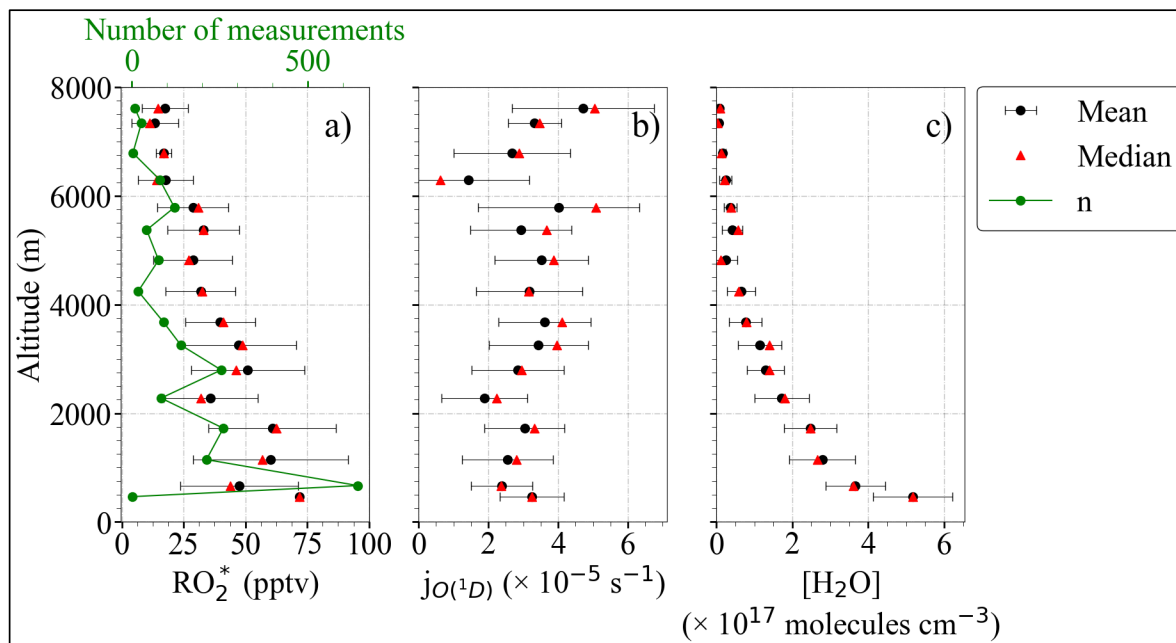
200 4.1. Airborne RO_2^* measurements during EMerGe in Europe

201 RO_2^* mixing ratios up to 120 pptv were measured during the campaign, as shown in Fig. 2. Typically, the highest RO_2^* mixing
 202 ratios were observed below 3000 m over Southern Europe. This is attributed to the higher insolation and temperatures favouring
 203 the rapid production of RO_2^* from the photochemical oxidations of CO and VOCs.



204
205 Figure 2: RO_2^* measured during EMeRGe-Europe: a) as a function of longitude and latitude, b) as a function of latitude and
206 altitude.

207 The origin and thus the composition of the air sampled during the seven flights over Europe were different and heterogeneous.
208 Typically, the air masses measured were influenced by emissions from MPCs and their surroundings, and sometimes by biomass
209 burning transported over short or long distances. The concentration and mixing ratio of RO_2^* depends on the insolation and the
210 chemical composition of the air masses probed, particularly on the abundance of RO_2^* precursors. Provided that insolation
211 conditions and a sufficient number of key participating precursors are comparable, the air mass origin is irrelevant for calculating
212 RO_2^* concentrations and mixing ratios. This is because the RO_2^* concentration is controlled by fast chemical and photochemical
213 processes. Thus, the RO_2^* variability and production rates provide insight into the photochemical activity of the air masses
214 probed. Changes in RO_2^* as a function of latitude and altitude, as shown in Fig. 2, confirm the heterogeneity of the
215 photochemical activity in the air masses probed. Figure 3 shows the RO_2^* vertical profiles averaged for the EMeRGe flights over
216 Europe in 500 m altitude bins. The error bars are standard errors (i.e. $\pm 1\sigma$ standard deviation of each bin). The vertical profiles
217 may be biased as the higher altitudes have fewer measurements than those below 3000 m, as mentioned in section 2. The vertical
218 profiles are a composite from averaging different flights and are shown to summarise the variability in the composition of the air
219 masses measured during the campaign.



220 Figure 3: Composite average vertical profiles of a) RO_2^* , b) $j_{\text{O}(^1\text{D})}$ and c) $[\text{H}_2\text{O}]$ observations. The measurements are binned over
 221 500 m altitude. The error bars are the standard errors (i.e. $\pm 1\sigma$ standard deviation of each bin). Median values (red triangles) and
 222 the number of individual measurements, n , for each bin (in green) are additionally plotted.
 223

224 Differences between mean and median values indicate less RO_2^* variability in the air masses probed above 3000 m. Most of the
 225 EMERGé measurements below 2000 m were carried out in the outflow of MPCs, which are expected to contain significant
 226 amounts of RO_2^* precursors. HALO flew at the lowest altitudes over the English Channel, the Mediterranean and the North Sea.
 227 The H_2O concentration in the air masses decreases steadily with altitude as expected. The higher relative variability in H_2O
 228 observed at 3000 m and the increase at 5000 m is associated with measurements under stormy conditions, often over the Alps.

229 4.2. RO_2^* production rates

230 The total production rate of OH and RO_2^* ($P_{\text{OH}+\text{HO}_2+\text{RO}_2^*}$) can be estimated from the reactions R1 to R13 as follows:

$$\begin{aligned}
 231 \quad P_{\text{OH}+\text{HO}_2+\text{RO}_2^*} &= 2j_{\text{O}_3}^1[\text{O}_3] \frac{k_{\text{O}_3+\text{H}_2\text{O}}[\text{H}_2\text{O}]}{k_{\text{O}_3+\text{H}_2\text{O}}[\text{H}_2\text{O}] + k_{\text{O}_3+\text{O}_2}[\text{O}_2] + k_{\text{O}_3+\text{N}_2}[\text{N}_2]} + j_{\text{HONO}}[\text{HONO}] + 2j_{\text{H}_2\text{O}_2}[\text{H}_2\text{O}_2] + 2\sum_i j_i[\text{OVOC}_i] + \\
 232 \quad &\sum_j k_{\text{OH}+\text{VOC}_j}[\text{OH}][\text{VOC}_j] + \sum_k k_{\text{O}_3+\text{alkenes}_k}[\text{O}_3][\text{alkenes}_k] \quad (\text{Eq. 2})
 \end{aligned}$$

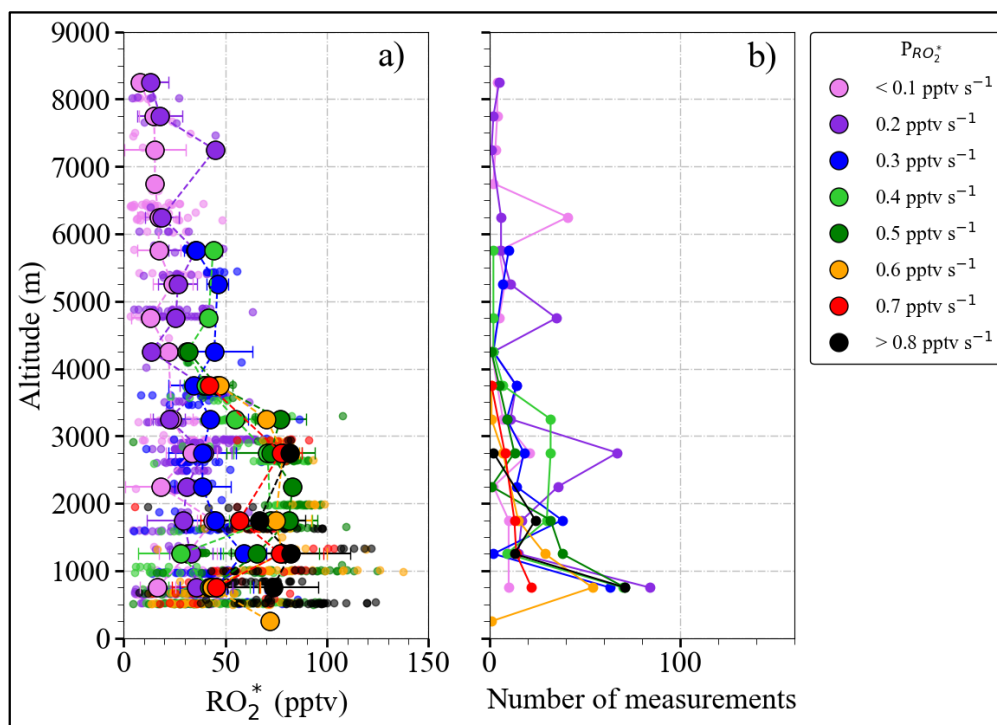
233 In this work, Eq. 2 has been applied to the measurements taken within the EMERGé campaign in Europe. There were no H_2O_2
 234 measurements available for EMERGé IOP. However, from the results reported by Tan et al. (2001), the OH production from the
 235 H_2O_2 photolysis become significant at low NO_x conditions. Since the $[\text{NO}_x] > 8 \times 10^{12}$ molecules cm^{-3} for 60 % of the
 236 measurements during the IOP, as a first approximation, the production of OH from H_2O_2 photolysis is assumed to be negligible
 237 for the dataset considered in this study. Similarly, the VOC photolysis was assumed to dominate the RO_2^* production over the
 238 oxidation by OH and ozonolysis of alkenes. The most abundant and reactive oxygenated volatile organic compounds (OVOCs)

239 measured have been taken as a surrogate for the sum of VOCs. These assumptions lead to Eq. 3, which estimates the RO_2^*
 240 production rate ($P_{RO_2^*}$) as:

$$241 \quad P_{RO_2^*} = 2j_{O(^1D)}[O_3] \frac{k_{O_B^+ + H_2O} [H_2O]}{k_{O_B^+ + H_2O} [H_2O] + k_{O_B^+ + O_2} [O_2] + k_{O_B^+ + N_2} [N_2]} + j_{HONO} [HONO] + 2j_{HCHO} [HCHO] + 2j_{CH_3CHO} [CH_3CHO] +$$

$$242 \quad 2j_{CH_3C(O)CH_3} [CH_3C(O)CH_3] + 2j_{CHOCHO} [CHOCHO] \quad (Eq.3)$$

243 Eq. 3 yields the rate of production of RO_2^* molecules. The production rate can be expressed in units of mixing ratio of RO_2^* by
 244 dividing with the air concentration at each altitude, estimated from the pressure and temperature measurements. Figure 4 shows
 245 the composite averaged vertical profile of all measured RO_2^* mixing ratios colour-coded with the estimated $P_{RO_2^*}$. Small circles
 246 show the 1-minute measurements binned for $P_{RO_2^*}$ up to 0.8 pptv s^{-1} in 0.1 pptv s^{-1} intervals. The production rates above 0.8 pptv s^{-1}
 247 s^{-1} are binned to the 0.8 pptv s^{-1} bin. Larger circles in the figure result from further binning the small circles over 500 m altitude
 248 steps. The error bars are the standard errors for each altitude bin. For the sake of representativeness and comparability, the
 249 number of measurements in each altitude bin is shown in Fig. 4b. Higher RO_2^* mixing ratios observed below 4000 m are
 250 typically associated with $P_{RO_2^*} \geq 0.4 \text{ pptv s}^{-1}$. Above 4000 m both $P_{RO_2^*}$ and RO_2^* start to decrease with altitude, as expected. This
 251 is related to the decrease in H_2O and other radical precursor concentrations with altitude, as detailed in Fig. 5 and Fig. 6. In
 252 previous airborne campaigns at various parts of the world, RO_2^* vertical distributions showed a local maximum between 1500
 253 and 4000 m , as reported by Tan et al. (2001), Cantrell et al. (2003a, 2003b), and Andrés-Hernández et al. (2009). In the present
 254 work, this local maximum is more evident for measurements with $P_{RO_2^*} \geq 0.5 \text{ pptv s}^{-1}$.



255
 256 Figure 4: a) Composite averaged vertical distribution of measured RO_2^* colour-coded according to the value of $P_{RO_2^*}$, b) the
 257 number of measurements in each altitude bin. Small circles are 1-minute individual measurements binned with $P_{RO_2^*}$ values in
 258 0.1 pptv s^{-1} intervals. Larger circles result from a further binning over 500 m altitude steps. All the production rates below 0.1 pptv s^{-1}
 259 s^{-1} and above 0.8 pptv s^{-1} are binned to 0.1 pptv s^{-1} and 0.8 pptv s^{-1} , respectively.

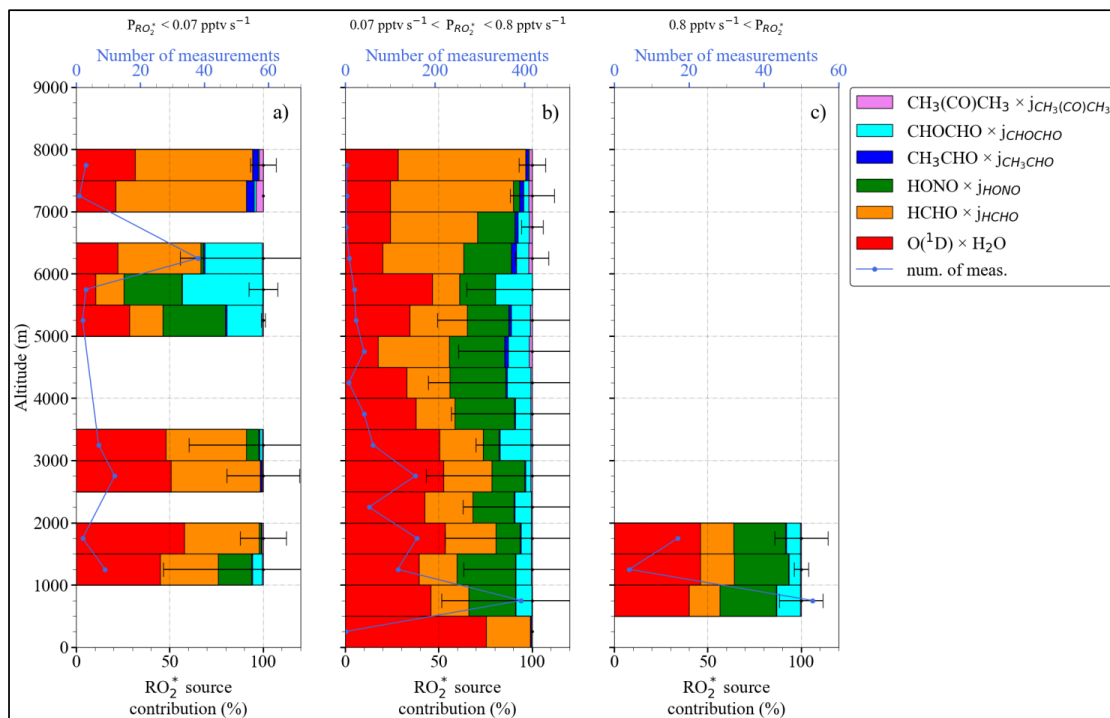


260 Figure 5 shows the fractional contribution of the production rate from each radical precursor reaction included in Eq. 3 as
261 a function of altitude. The data are classified into three groups according to the rate of change of production of the RO_2^* mixing
262 ratio $P_{\text{RO}_2^*} < 0.07 \text{ pptv s}^{-1}$ (5a), $0.07 < P_{\text{RO}_2^*} < 0.8 \text{ pptv s}^{-1}$ (5b), and $P_{\text{RO}_2^*} > 0.8 \text{ pptv s}^{-1}$ (5c) to show the lowest, most common,
263 and highest ranges, respectively, encountered during the IOP. For 89 % of the measurements, $0.07 < P_{\text{RO}_2^*} < 0.8 \text{ pptv s}^{-1}$ applies,
264 while the rest of the data are equally distributed in the other two $P_{\text{RO}_2^*}$ ranges. The data in each group are always binned over 500
265 m when available.

266 Typically, the high amount of H_2O in the air masses probed results in the O_3 photolysis and subsequent reaction of $\text{O}(^1\text{D})$ with
267 H_2O (R1-R2a) and is the highest RO_2^* radical production rate ($\geq 50 \%$) below 4000 m. As the amount of H_2O reduces with
268 altitude, the relative contribution from O_3 photolysis decreases. Above 4000 m, HCHO, HONO, and CHOCHO photolysis
269 contributions range between 20 % to 40 %, 2.5 % to 30 %, and 5 % to 25 %, respectively. The HCHO contribution increases up
270 to 80% during measurements above 6000 m. The contributions of CH_3CHO and $\text{CH}_3\text{C}(\text{O})\text{CH}_3$ photolysis are, in contrast,
271 practically negligible ($< 5 \%$).

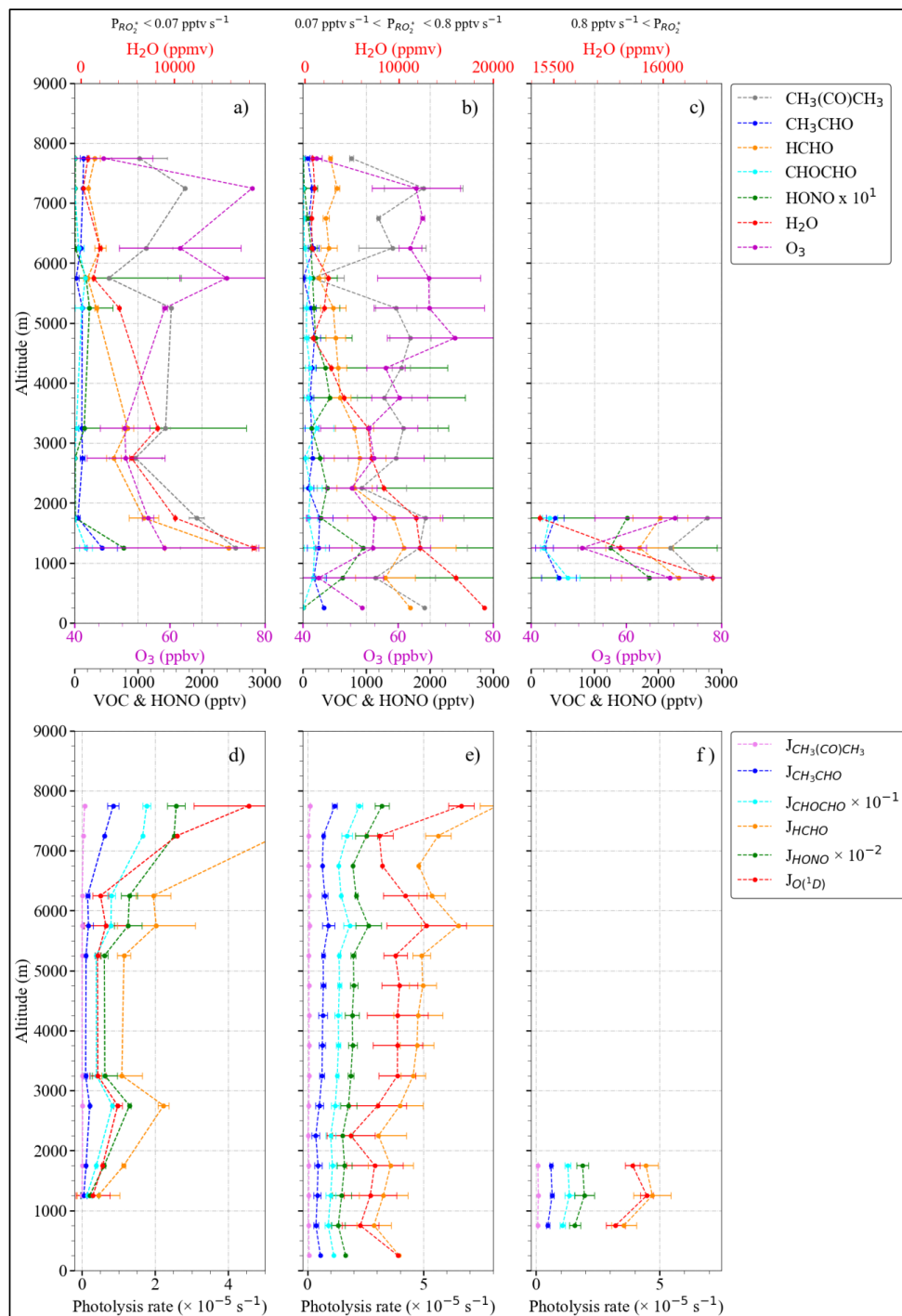
272 The vertical changes of the precursor mixing ratios and photolysis frequencies used to calculate $P_{\text{RO}_2^*}$ in Fig. 5 are shown in Fig.
273 6a to 6f. $P_{\text{RO}_2^*} < 0.07 \text{ pptv s}^{-1}$ is associated with measurements under cloudy conditions, towards sunset where the photolysis
274 frequencies are low, or at altitudes above 5000 m in air masses with a low amount of RO_2^* precursors. $P_{\text{RO}_2^*} > 0.8 \text{ pptv s}^{-1}$ are
275 found for air masses, measured below 2000 m in the outflow of MPCs over the sea, for conditions having sufficient insolation
276 ($j_{\text{O}(^1\text{D})} > 3 \times 10^{-5} \text{ s}^{-1}$) and a high content of RO_2^* precursors (HCHO $> 1000 \text{ pptv}$ and HONO $> 100 \text{ pptv}$). The increase in the
277 photolysis frequencies as a function of altitude is concurrent with decreases in precursor concentrations. As a result, the $P_{\text{RO}_2^*}$ do
278 not significantly vary with altitude in the air masses investigated.

279 In previous airborne campaigns, Tan et al. (2001) and Cantrell et al. (2003b) reported a reduction of the fractional contribution of
280 the reaction of $\text{O}(^1\text{D})$ with H_2O as the $P_{\text{RO}_2^*}$ value decreases. At very low $P_{\text{RO}_2^*}$ values ($< 0.03 \text{ pptv s}^{-1}$), the sum of all other
281 production terms exceeded the fraction from the $\text{O}(^1\text{D}) + \text{H}_2\text{O}$ term. For these conditions, H_2O_2 and VOCs photolysis dominated
282 the $P_{\text{RO}_2^*}$. In the case of the EMERGe data set in Europe, only 6 % of $P_{\text{RO}_2^*}$ are below 0.06 pptv s^{-1} .



283

284 Figure 5: Total $P_{RO_2^*}$ and fractional precursor contributions estimated using Eq. 5 as a function of altitude, for: a) $P_{RO_2^*} < 0.07$
285 pptv s^{-1} , b) $0.07 \text{ pptv s}^{-1} < P_{RO_2^*} < 0.8 \text{ pptv s}^{-1}$, and c) $P_{RO_2^*} > 0.8 \text{ pptv s}^{-1}$. Note the different scales in the number of
286 measurements.



287

288 Figure 6: Vertical distribution and variation of a) to c) precursor mixing ratios; d) to f) photolysis frequencies for the P_{RO_2} bins
 289 as in Fig. 5. Note the different scales in the H_2O concentration

290



291 4.3. PSS estimation of RO_2^* mixing ratios

292 Under most ambient conditions in the troposphere, the RO_2^* , which to a first approximation is the sum of HO_2 and RO_2 , are
293 short-lived, and the chemical lifetime of RO_2^* is much shorter than the chemical transport time into and out of an air mass being
294 probed. Consequently, pseudo-steady-state conditions prevail, and the radical production and loss rates are balanced:

295

$$296 P_{\text{HO}_2+\text{RO}_2} = L_{\text{HO}_2+\text{RO}_2} \quad (\text{Eq.4})$$

297 If the interconversion reactions between OH, RO, HO_2 and RO_2 (R5 to R7, R12, R16b, and R23 to R26) occur without losses,
298 then the radical number concentrations are calculated by solving Eq. 4. If the $\text{RO}_2^* - \text{RO}_2^*$ reactions are assumed to be the
299 dominant radical loss processes, Eq. 4 leads to Eq. 5.

$$2j_{\text{O}(^1\text{D})}[\text{O}_3] \frac{k_{\text{O}_3+\text{H}_2\text{O}}[\text{H}_2\text{O}]}{k_{\text{O}_3+\text{H}_2\text{O}}[\text{H}_2\text{O}] + k_{\text{O}_3+\text{O}_2}[\text{O}_2] + k_{\text{O}_3+\text{N}_2}[\text{N}_2]} + j_{\text{HONO}}[\text{HONO}] + 2j_{\text{HCHO}}[\text{HCHO}] + 2j_{\text{CH}_3\text{CHO}}[\text{CH}_3\text{CHO}] \\ + 2j_{\text{CH}_3\text{C(O)CH}_3}[\text{CH}_3\text{C(O)CH}_3] + 2j_{\text{CHOCHO}}[\text{CHOCHO}] = k_{\text{RO}_2^*+\text{RO}_2^*}[\text{RO}_2^*]^2$$

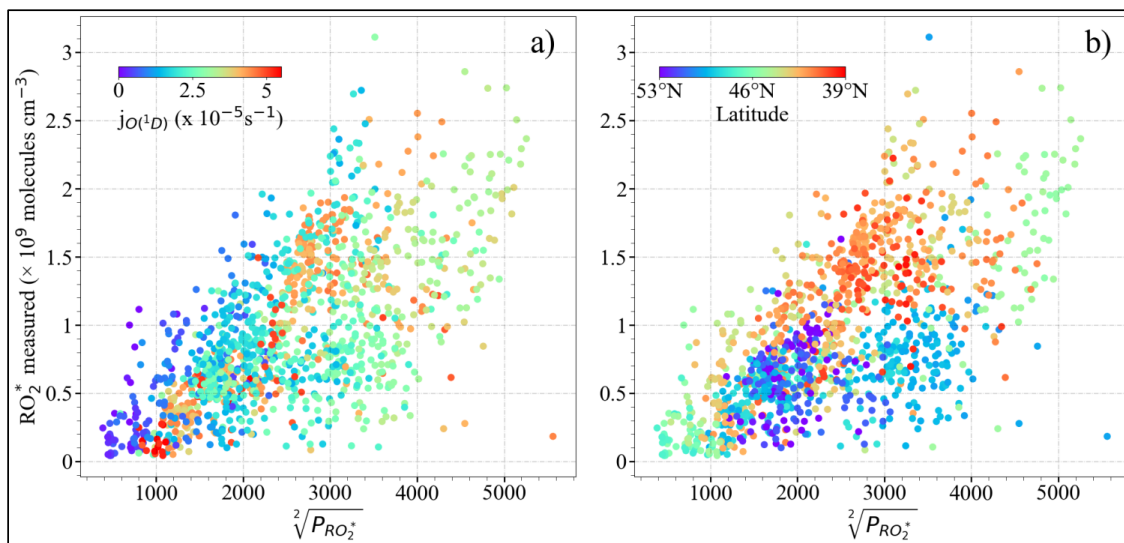
300

(Eq. 5)

301 where $k_{\text{RO}_2^*+\text{RO}_2^*}$ is the effective RO_2^* self-reaction rate coefficient, which is defined as the weighted average rate coefficient
302 between $\text{HO}_2 - \text{HO}_2$, $\text{HO}_2 - \text{RO}_2$ and $\text{RO}_2 - \text{RO}_2$ reactions.

303 Consequently, the RO_2^* concentrations are expected to correlate with the square root of the $P_{\text{RO}_2^*}$.

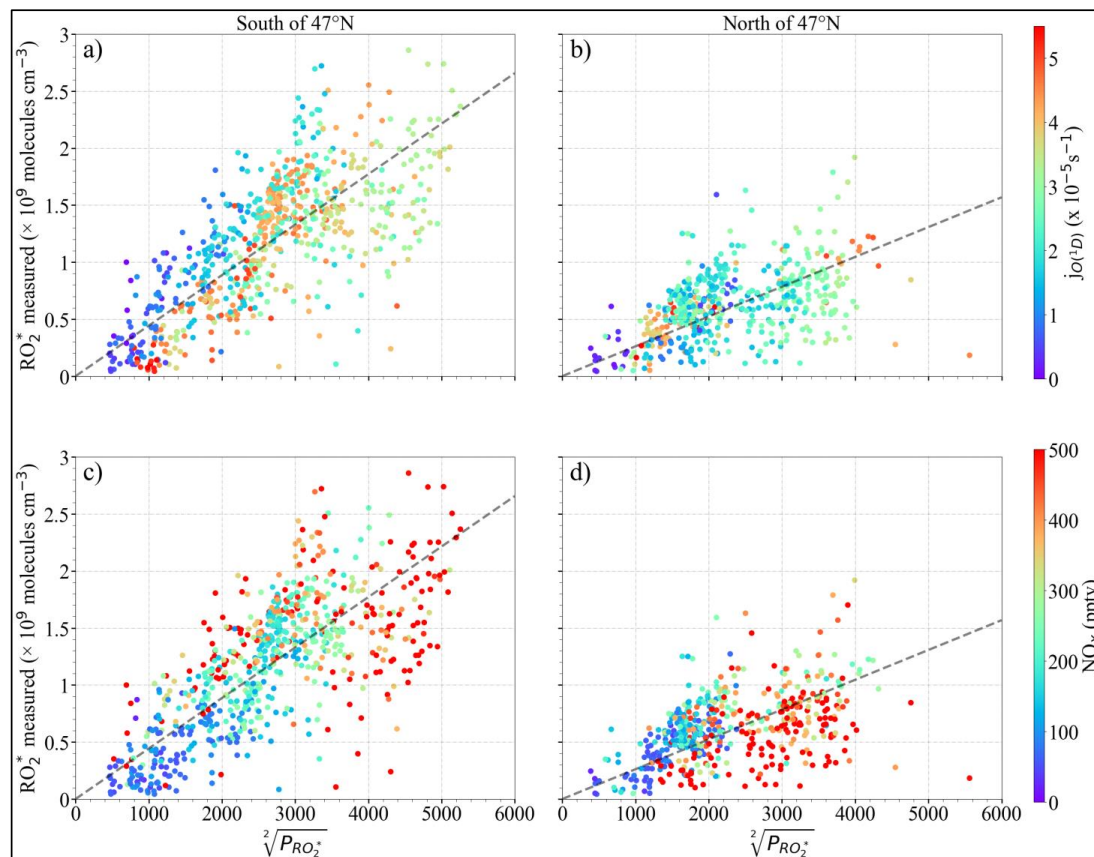
304 Figure 7 shows the relationship between the measured $[\text{RO}_2^*]$ and the estimated $\sqrt{P_{\text{RO}_2^*}}$. Generally, both $[\text{RO}_2^*]$ and $\sqrt{P_{\text{RO}_2^*}}$
305 increase with the photolysis frequency of O_3 ($j_{\text{O}(^1\text{D})}$). The $[\text{RO}_2^*] < 0.5 \times 10^{12}$ molecules cm^{-3} and $\sqrt{P_{\text{RO}_2^*}} < 1000$ with $j_{\text{O}(^1\text{D})} > 5$
306 $\times 10^{-5}$ belong to the measurements made above 6000 m, where the amount of RO_2^* precursors is low. The relatively weak
307 correlation observed between $[\text{RO}_2^*]$ and $\sqrt{P_{\text{RO}_2^*}}$ indicates the presence of other radical loss processes and/or missing production
308 terms in the $P_{\text{RO}_2^*}$ calculation. Apart from this, the spread in the diagram confirms that the effective RO_2^* self-reaction rate
309 $k_{\text{RO}_2^*+\text{RO}_2^*}[\text{RO}_2^*]^2$ varies widely in the air masses probed due to the effect of changes in HO_2 and ΣRO_2 concentrations in the
310 individual loss reaction rate coefficients. As mentioned in section 4.1, photochemical processing was expected to be enhanced
311 over Southern Europe due to the prevailing high insolation and temperatures during the measurements. This is also reflected in
312 the higher $P_{\text{RO}_2^*}$ and $[\text{RO}_2^*]$ observed in Southern Europe as compared to those in Northern Europe (Fig. 7b).



313

314 Figure 7: Plot of the measured $[\text{RO}_2^*]$ versus estimated $\sqrt{P_{\text{RO}_2^*}}$ colour-coded for values of a) $j_{\text{O}(^1\text{D})}$ and b) latitude.

315 The correlation between $[\text{RO}_2^*]$ and $\sqrt{P_{\text{RO}_2^*}}$ improves when the measurements south and north of 47°N are separately analysed
316 (Fig. 8). For a given $[\text{RO}_2^*]$, the $P_{\text{RO}_2^*}$ calculated is higher for the measurements north of 47°N than south of 47°N . The lowest
317 $[\text{RO}_2^*]$ to $\sqrt{P_{\text{RO}_2^*}}$ ratios are associated with higher NO_x ($\text{NO} + \text{NO}_2$), especially north of 47°N , indicating the urban character and
318 higher content in RO_2^* precursors of the air probed (Fig. 8d). Note that these results are only valid for the data set acquired over
319 Europe during EMERGE and do not yield a relationship between $[\text{RO}_2^*]$ and $\sqrt{P_{\text{RO}_2^*}}$, which is generally applicable for these two
320 latitude windows.



321
 322 Figure 8: Plots of the measured $[\text{RO}_2^*]$ vs $\sqrt{P_{\text{RO}_2^*}}$ for the following latitudes: a) and c) south of 47°N ; b) and d) north of 47°N .
 323 Note that a) and b) are colour-coded with $j_{\text{O}(^1\text{D})}$; c) and d) are colour-coded by NO_x mixing ratio. The dashed lines indicate the
 324 linear fit for visual support.

325 The relationship between RO_2^* and $P_{\text{RO}_2^*}$ is further investigated to identify the dominant RO_2^* loss process in the air masses
 326 considered in this study. As stated in section 3, HO_2 and RO_2 are not speciated but retrieved as RO_2^* by the PerCEAS
 327 instrument. So, the effect of changes in the HO_2 to the total RO_2^* ratios, represented by δ , i.e., $[\text{HO}_2] = \delta[\text{RO}_2^*]$ and $[\text{CH}_3\text{O}_2] =$
 328 $(1 - \delta)[\text{RO}_2^*]$, is investigated. As a first approach, CH_3O_2 reactions are taken as a surrogate for all RO_2 reactions to reduce the
 329 complexity of the calculations. Consequently, Eq. 5 is accordingly modified:

$$\begin{aligned}
 330 \quad & 2j_1[\text{O}_3]\beta + j_3[\text{HONO}] + 2j_8[\text{HCHO}] + 2j_9[\text{CH}_3\text{CHO}] + 2(j_{10a} + j_{10b})[\text{CH}_3\text{C}(\text{O})\text{CH}_3] + 2j_{11}[\text{CHOCHO}] = 2k_{15}\delta(1 - \\
 331 \quad & \delta)[\text{RO}_2^*]^2 + 2k_{16a}((1 - \delta)[\text{RO}_2^*])^2 + 2k_{14}(\delta[\text{RO}_2^*])^2 \quad (\text{Eq. 6})
 \end{aligned}$$

332 where β is the effective yield of OH production in the reaction of $\text{O}(^1\text{D})$ with H_2O given by:

$$333 \quad \beta = \left(\frac{k_{2a}[\text{H}_2\text{O}]}{k_{2a}[\text{H}_2\text{O}] + k_{2b}[\text{O}_2] + k_{2c}[\text{N}_2]} \right)$$

334 From Eq. 6, $[\text{RO}_2^*]$ can be calculated as



$$[\text{RO}_2^*] = \sqrt{\frac{P_{\text{RO}_2^*}}{2k_{\text{RO}_2^*}}} \quad (\text{Eq. 7})$$

where

$$k_{\text{RO}_2^*} = (k_{15}\delta(1-\delta) + k_{16a}(1-\delta)^2 + k_{14}\delta^2)$$

$$P_{\text{RO}_2^*} = 2j_1[\text{O}_3]\beta + j_3[\text{HONO}] + 2j_8[\text{HCHO}] + 2j_9[\text{CH}_3\text{CHO}] + 2(j_{10a} + j_{10b})[\text{CH}_3\text{C}(\text{O})\text{CH}_3] + 2j_{11}[\text{CHOCHO}]$$

The second solution gives negative values for $[\text{RO}_2^*]$, therefore has no physical meaning. A more detailed derivation of Eq. 6 and Eq. 7 are given in the supplementary information.

Figure 9 shows the measured RO_2^* ($\text{RO}_2^*_m$) mixing ratio versus the calculated RO_2^* ($\text{RO}_2^*_c$) mixing ratio using Eq. 7, colour-coded with respect to the NO mixing ratios. $\text{RO}_2^*_m$ and $\text{RO}_2^*_c$ are the measured and calculated RO_2^* respectively for $\delta = 1$, i.e. $\text{RO}_2^* = \text{HO}_2$ and $\delta = 0.5$, i.e. $\text{HO}_2 = \text{RO}_2$. The eCL corresponding to $\delta = 1$ and $\delta = 0.5$ used for the $\text{RO}_2^*_m$ retrievals were determined in laboratory experiments, as reported by George et al. (2020). The small circles represent 1-minute $\text{RO}_2^*_m$, whereas the large circles are the mean of the $\text{RO}_2^*_m$ binned over 10 pptv $\text{RO}_2^*_c$ intervals. Despite the limited number of production and loss processes considered, $\text{RO}_2^*_c$ reasonably agrees with $\text{RO}_2^*_m$ as indicated by the fit parameters (Table 2). $\text{RO}_2^*_c$ often overestimates $\text{RO}_2^*_m$ for NO mixing ratios above 250 pptv. The overestimation is also evident for $\text{RO}_2^*_m$ below 40 pptv. This may be due to the HO and RO losses during the radical interconversion by reacting with NO_x producing HONO, HNO_3 and organic nitrate.

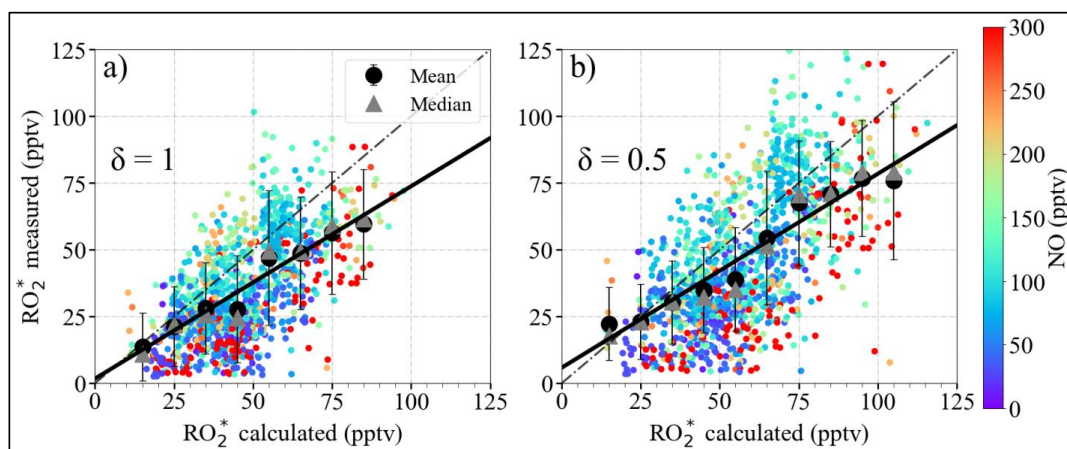


Figure 9: RO_2^* measured ($\text{RO}_2^*_m$) versus PSS RO_2^* calculated ($\text{RO}_2^*_c$) using Eq. 7 for a) $\delta = 1$, b) $\delta = 0.5$ by assuming only $\text{RO}_2^* - \text{RO}_2^*$ loss reactions. The 1-minute (small circles), the mean of the binned $\text{RO}_2^*_m$ over 10 pptv $\text{RO}_2^*_c$ intervals (large circles), and the median of each bin (grey triangles) are shown. The error bars indicate the standard error of each bin. The linear regression for the binned values (solid line) and the 1:1 relation (dashed line) are also plotted for reference. The fit parameters are given in Table 2.

The PSS data presented in Fig. 9 are calculated assuming interconversion reactions between OH, RO and RO_2^* occur without losses and the limiting case of $[\text{OH}] \ll [\text{HO}_2 + \text{RO}_2^*]$ in the case of a low amount of NO and NO_2 . Furthermore, VOC oxidation processes are not considered as a source of radicals. To identify other major loss processes, Eq. 6 is extended with radical conversion reactions between oxy and peroxy radicals and OH and RO losses through HONO, HNO_3 , and organic nitrate



359 formation. In the resulting Eq. 8, CH₄, HCHO, CH₃CHO, CHOCHO, CH₃OH, and CH₃C(O)CH₃ measured on-board HALO are
 360 taken as surrogates for the dominant VOC acting as RO₂^{*} precursors through oxidation:

$$\begin{aligned}
 & (2j_1[O_3]\beta + j_3[HONO])(1 - \rho) + 2j_8[HCHO] + 2j_9[CH_3CHO] + 2(j_{10a} + j_{10b})[CH_3C(O)CH_3] + 2j_{11}[CHOCHO] = \\
 & \delta[RO_2^*](k_{23}[NO] + k_{24}[O_3])\rho + \left(2k_{16b}((1 - \delta)[RO_2^*])^2 + k_{25}(1 - \delta)[RO_2^*][NO]\right) \left(\frac{k_{22}[NO]}{(k_{22}[NO] + k_{26}[O_2])}\right) + 2k_{15}\delta(1 - \\
 & \delta)[RO_2^*]^2 + 2k_{16a}((1 - \delta)[RO_2^*])^2 + 2k_{14}(\delta[RO_2^*])^2 \quad (\text{Eq. 8})
 \end{aligned}$$

364 where β is the OH production efficiency of the O₃ photolysis and δ is the HO₂ to RO₂^{*} ratio as in Eq. 6, ρ is the OH loss during
 365 the OH – RO₂^{*} interconversion. As in Eq. 6, CH₃O₂ is taken as a surrogate for all RO₂. The detailed derivation of Eq. 8 is given
 366 in the supplementary information.

367 During the IOP in Europe, HCHO and CH₃CHO are the dominant radical precursors from OVOC oxidations. Their impact on
 368 the radical budget is similar because their respective concentrations compensate the difference in the rate coefficients of their
 369 reactions with OH ($k_{OH+HCHO} = 8.5 \times 10^{-12} \text{ cm}^3 \text{ molecule}^{-1} \text{ s}^{-1}$ and $k_{OH+CH_3CHO} = 1.5 \times 10^{-11} \text{ cm}^3 \text{ molecule}^{-1} \text{ s}^{-1}$). Despite the
 370 high mixing ratios measured, CH₃C(O)CH₃ is a less important source of RO₂^{*}. This is because the rate coefficient
 371 $k(T)_{OH+CH_3C(O)CH_3}$ is significantly slower than $k_{OH+HCHO}$ and k_{OH+CH_3CHO} (see Table S1 in the supplement). Similarly, the
 372 RO₂^{*} production rate of CHOCHO and CH₃OH through oxidation is an order of magnitude lower than that of HCHO and
 373 CH₃CHO. Since $k_{HO_2+O_3}$ is almost four orders of magnitude smaller than k_{HO_2+NO} and the NO concentrations remained about
 374 three orders of magnitude smaller than the O₃ measured, the HO₂ reaction with O₃ had a negligible effect in Eq. 8.

375 The impact of the methylglyoxal (CH₃C(O)C(O)H) photolysis was also investigated by using the CH₃C(O)C(O)H^{*}
 376 measurements provided by the miniDOAS instrument. The CH₃C(O)C(O)H^{*} measured is the sum of CH₃C(O)C(O)H, and a
 377 fraction of other substituted dicarbonyls (mainly 2,3-butanedione, C₄H₆O₂), with similar visible absorption spectra. For the
 378 calculation, CH₃C(O)C(O)H was assumed to be half of CH₃C(O)C(O)H^{*} as recommended by Zarzana et al. (2017) and Kluge et
 379 al. (2020). The RO₂^{*} calculated by including CH₃C(O)C(O)H photolysis systematically overestimated the measurements. Since
 380 the adequacy of the recommended factor of 0.5 varies with the actual air mass composition, CH₃C(O)C(O)H was not included in
 381 the calculations.

382 The revised PSS [RO₂^{*}] is then calculated from Eq. 8, as:

$$[RO_2^*] = \frac{-(-L_{RO_2^*}) - \sqrt{L_{RO_2^*}^2 - 4(-2k_{RO_2^*})P_{RO_2^*}}}{2(-2k_{RO_2^*})} \quad (\text{Eq. 9})$$

384 where

$$\begin{aligned}
 k_{RO_2^*} &= \left(k_{16b} \left(\frac{k_{22}[NO]}{(k_{22}[NO] + k_{26}[O_2])} \right) + k_{16a} \right) (1 - \delta)^2 + k_{15}\delta(1 - \delta) + k_{14}\delta^2 \\
 L_{RO_2^*} &= \left(\delta(k_{23}[NO] + k_{24}[O_3])\rho + \left(\frac{k_{22}[NO]}{(k_{22}[NO] + k_{26}[O_2])} \right) k_{25}(1 - \delta)[NO] \right) \\
 P_{RO_2^*} &= (2j_1[O_3]\beta + j_3[HONO])(1 - \rho) + 2j_8[HCHO] + 2j_9[CH_3CHO] + 2(j_{10a} + j_{10b})[CH_3C(O)CH_3] + 2j_{11}[CHOCHO]
 \end{aligned}$$

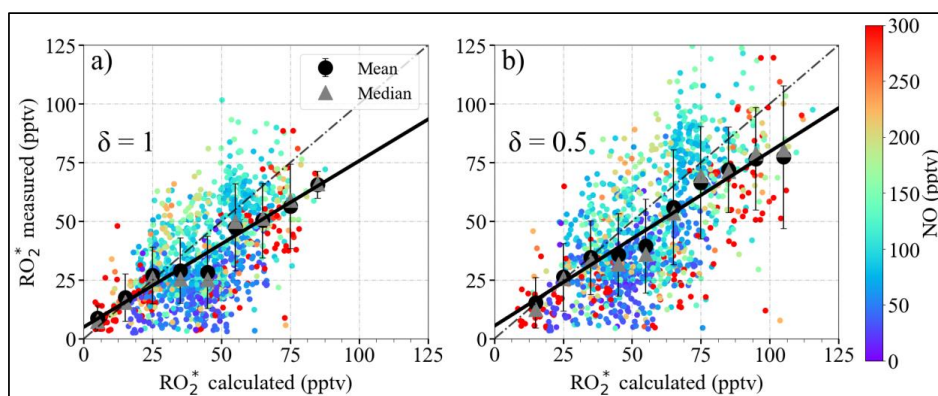
386 Applying Eq. 9 to the measured dataset reduces the overestimation of RO₂^{*}_m by RO₂^{*}_c at NO mixing ratios higher than 250 pptv
 387 (Fig. 10), especially for RO₂^{*}_m < 40 pptv but does not introduce significant changes in the overall correlations (Table 2). As in



388 Fig. 9, plots of the 1-minute $RO_2^*_m$ and the average of $RO_2^*_m$ binned over 10 pptv $RO_2^*_c$ intervals versus $RO_2^*_c$ are depicted for δ
 389 = 1 and $\delta = 0.5$ in Fig. 10. The RO_2^* data are colour-coded with the on-board NO measurements. The linear regression slopes are
 390 around 0.7 ($R^2 = 0.96$), indicating an overall 25 – 30 % underestimation of the $RO_2^*_m$. However, the $RO_2^*_m$ are mostly
 391 overestimated 4000 m under low insolation and underestimated in polluted plumes measured below 2000 m with NO mixing
 392 ratios approximately above 50 pptv (see Fig. 11 for $\delta = 0.5$). The y-axis intercept is below the instrumental detection limit for
 393 most measurement conditions.

394 Table 2: Linear regression parameters from $RO_2^*_m$ versus $RO_2^*_c$ using Eq. 7 and Eq. 9 from Fig. 9 and Fig.10, respectively.

Formula used to calculate RO_2^*	δ	slope	y-intercept (pptv)	R^2
Eq. 7	1.00	0.72	2	0.96
	0.50	0.73	6	0.96
Eq. 9	1.00	0.71	5	0.96
	0.50	0.74	6	0.97



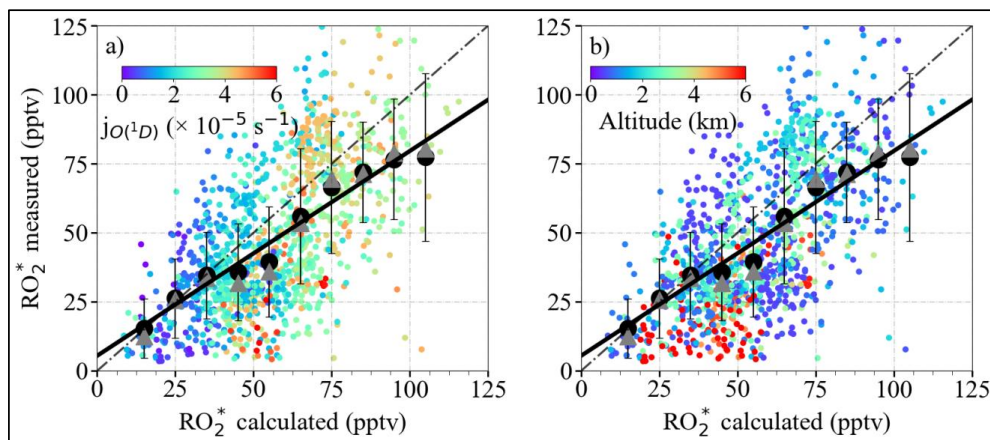
395

396 Figure 10: $RO_2^*_m$ versus $RO_2^*_c$ calculated using Eq. 9 for a) $\delta = 1$ and b) $\delta = 0.5$. The data are colour-coded with the measured
 397 NO mixing ratios. The 1-minute (small circles), the mean of the binned $RO_2^*_m$ over 10 pptv $RO_2^*_c$ intervals (large circles), and
 398 the median of each bin (grey triangles) are shown. The error bars indicate the standard error of each bin. The linear regression for
 399 the binned values (solid line) and the 1:1 relation (dashed line) are also depicted for reference.

400

401

402

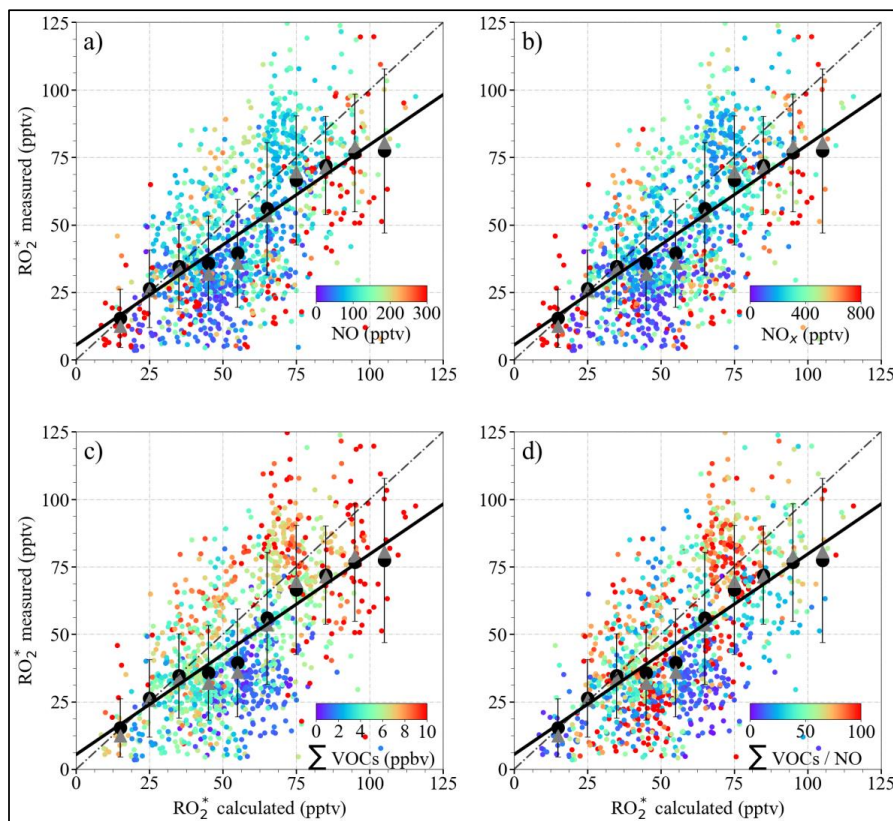


403

404 Figure 11: RO_2^* versus RO_2^* calculated using Eq. 9 for $\delta = 0.5$. The data points are colour-coded for a) photolysis frequency of
405 O_3 ; b) altitude. The 1-minute (small circles), the mean of the binned RO_2^* over 10 pptv RO_2^* intervals (large circles), and the
406 median of each bin (grey triangles) are shown. The error bars indicate the standard error of each bin. The linear regression for the
407 binned values (solid line) and the 1:1 relation (dashed line) are also depicted for reference.

408 Figure 12 shows the data for $\delta = 0.5$ colour-coded with NO , NO_x , the sum of $HCHO$, CH_3CHO , $CHOCHO$, CH_3OH , and
409 $CH_3C(O)CH_3$ (from now on referred to as $\Sigma VOCs$), as a surrogate for the amount of $OVOCs$ acting as RO_2^* precursors, and the
410 $\Sigma VOCs$ to NO ratio. The largest differences between RO_2^* and RO_2^* is observed for the bins around 50 pptv. The RO_2^* < 25
411 pptv observed above 4000 m are overestimated for air masses with low insolation, i.e. $j_{O(^1D)} < 2 \times 10^{-5} s^{-1}$ (Fig. 11), $NO < 50$
412 pptv, $\Sigma VOCs$ typically below 4 ppbv, and high $\Sigma VOCs/NO$ ratios (> 50). Under these insolation conditions, the radical
413 production rate is expected to be low, and the $RO_2^* - RO_2^*$ reactions are expected to dominate the RO_2^* loss processes. Since OH
414 and H_2O_2 were not measured during the EMeRGe campaign in Europe, Eq. 9 does not include the loss reactions R17 and R18,
415 which might be significant under such conditions and explain the RO_2^* overestimation. This is also the case for the
416 overestimations observed below 40 pptv RO_2^* at other altitudes, where $NO < 50$ pptv but the $\Sigma VOCs/NO$ ratios remain low.
417 The overestimation may therefore be independent of the $\Sigma VOCs/NO$ ratios. For $NO \leq 50$ pptv, $NO_2 \leq 100$ pptv, $RO_2^* \leq 40$ pptv
418 and $HCHO \leq 1$ ppbv, the rate of reaction R18, which forms H_2O and O_2 from OH and HO_2 , is about 4 times faster than the rate
419 of the OH oxidation reaction of the dominant $OVOCs$ (R12) considered in this study or the rate of formation of $HONO$ (R19).

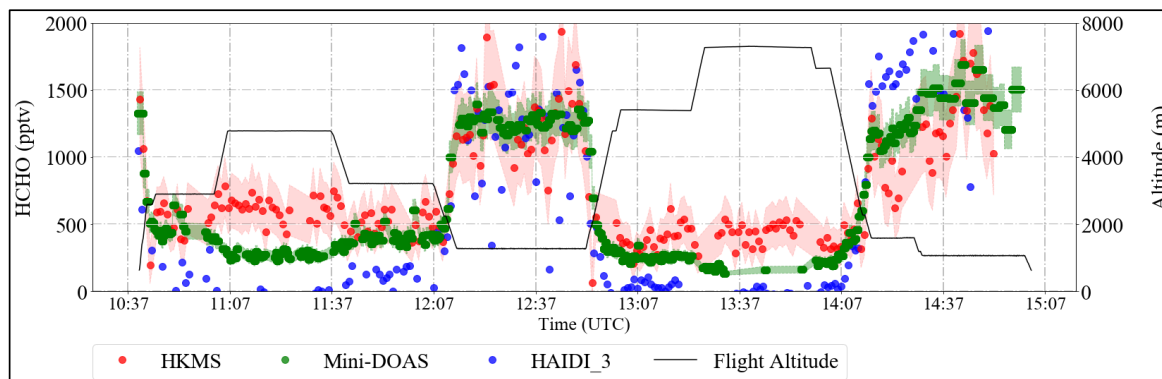
420 RO_2^* is systematically underestimated for $\Sigma VOCs$ greater than 7 ppbv. The composition of these air masses is quite different,
421 as reflected by the $\Sigma VOCs/NO$ ratios. This implies that Eq. 9 does not capture the peroxy radical production adequately from
422 $VOCs$ in these cases. The underestimation of RO_2^* may be explained in part by a) OH recycling through additional VOC
423 oxidation processes, which are not in Eq. 9 and/or b) RO_2^* production from the photolysis of carbonyls, which were not
424 measured and/or c) RO_2^* production from the ozonolysis of alkenes.



425

426 Figure 12: $RO_2^*{}_m$ versus $RO_2^*{}_c$ using Eq. 9 for $\delta = 0.5$ colour-coded with the measured a) NO mixing ratio, b) NO_x mixing ratio,
427 c) $\Sigma VOCs$ mixing ratio, where $\Sigma VOCs = HCHO + CH_3CHO + (CHO)_2 + CH_3OH + CH_3C(O)CH_3$, and d) $\Sigma VOCs/NO$ ratio. The
428 1-minute (small circles), the mean of the binned $RO_2^*{}_m$ over 10 pptv $RO_2^*{}_c$ intervals (large circles), and the median of each bin
429 (triangles) are shown. The error bars represent the standard error of each bin. The linear regression for the binned values (solid
430 line) and the 1:1 relationship (dashed line) are plotted for reference.

431 Spatial and temporal differences in the in-situ measurements of the key trace gases (O_3 , NO, H_2O , CO, CH_4 , VOCs) with respect
432 to remote sensing observations (NO_2 and HONO) used in Eq. 9 may also contribute to the overall spread observed in Fig. 12.
433 Although the temporal evolution and the amount of the trace gases measured using in-situ and remote sensing instruments agree
434 reasonably well, as shown for HCHO in Fig.13, the remote sensing instruments have, in general, larger air sampling volumes
435 compared to that of in-situ instruments. This may occasionally lead to significant differences depending on the location of the
436 pollutant layers with respect to HALO. In addition, PTR-MS measurements of HCHO might include interferences from
437 molecular fragments of other compounds in the sample air (Inomata et al., 2008). Further details about the accuracy and
438 comparability of the instrumentation on-board during the campaign can be found elsewhere (Schumann, 2020).

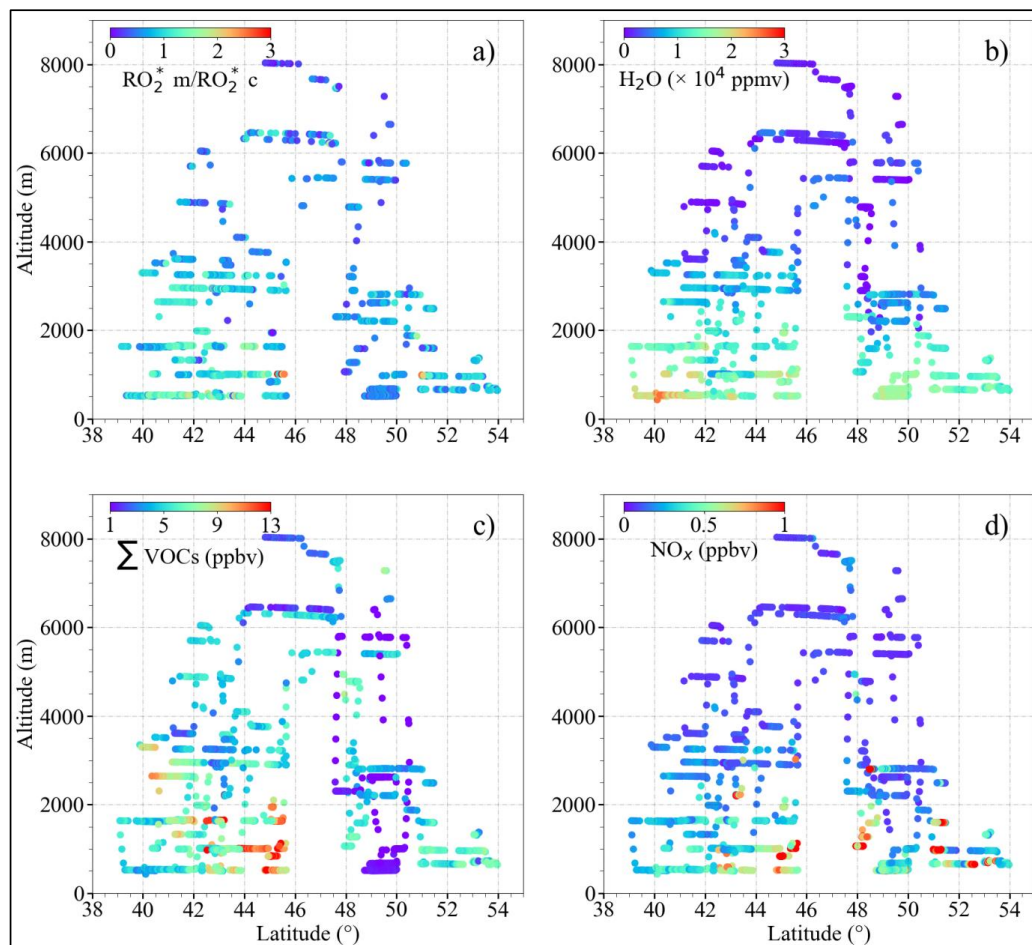


439

440 Figure 13: An example of the time series of the measured HCHO mixing ratios retrieved from the remote sensing (HAIDI in blue
441 and miniDOAS in green) and in-situ (HKMS in red) instruments during the E-EU-04 flight on 14.07.2017. The shaded region
442 shows $\pm 1\sigma$ uncertainties of the HKMS and miniDOAS instruments. The flight altitude is depicted in black.

443 In summary, the differences between $RO_2^*_m$ and $RO_2^*_c$ might be caused by a combined effect of the limitations of the analytical
444 expression to simulate complex non-linear chemistry and the measurement uncertainties arising from the spatial heterogeneity of
445 the plume for the remote sensing instruments. Consequently, individual analysis of the pollution events encountered along the
446 flights is required to quantify limiting factors in Eq. 9.

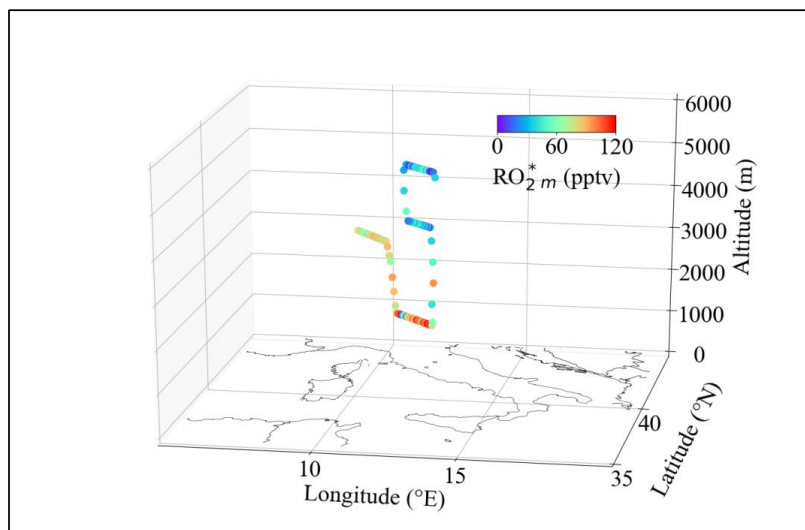
447 The ratio of $RO_2^*_m$ to $RO_2^*_c$ ($RO_2^*_m/RO_2^*_c$) has been used to assess the applicability of Eq. 9 for the calculation of RO_2^* in the air
448 masses probed (Fig. 14). In Fig. 14, the data are colour-coded with respect to $RO_2^*_m/RO_2^*_c$, H_2O , $\Sigma VOCs$, and NO_x . The air
449 masses probed at altitudes above 2000 m are close to the PSS assumptions used to develop Eq. 9, and consequently, the
450 $RO_2^*_m/RO_2^*_c$ remains ≤ 1 . In contrast, $RO_2^*_m/RO_2^*_c$ is at its highest value below 2000 m, reaching up to 3. At these altitudes,
451 most of the flights in Europe were carried out in pollution plumes, in which both the amount of NO_x and RO_2^* precursors are
452 high. The analytical expression does not capture the RO_2^* variations resulting from fast non-linear photochemistry present in
453 these pollution plumes. This is the case for the measurements made between $42^\circ N$ and $46^\circ N$ in the outflow of Po Valley and
454 Rome. $\Sigma VOCs > 7$ ppbv and NO_x mixing ratios > 500 pptv indicate high radical precursor loading and relatively fresh
455 emissions. The $RO_2^*_m/RO_2^*_c$ is also > 2 in the measurements over the English Channel (between $50^\circ N$ and $52^\circ N$) with $\Sigma VOCs$
456 and NO_x mixing ratio > 7 ppbv and 1000 pptv, respectively.



457

458 Figure 14: Plots of a) the ratio of $RO_2^* m$ to $RO_2^* c$ ($RO_2^* m/RO_2^* c$) assuming that $\delta = 0.5$; b) H_2O ; c) $\sum VOCs$; d) NO_x as a function
459 of latitude and altitude for the EMERGE measurements in Europe.

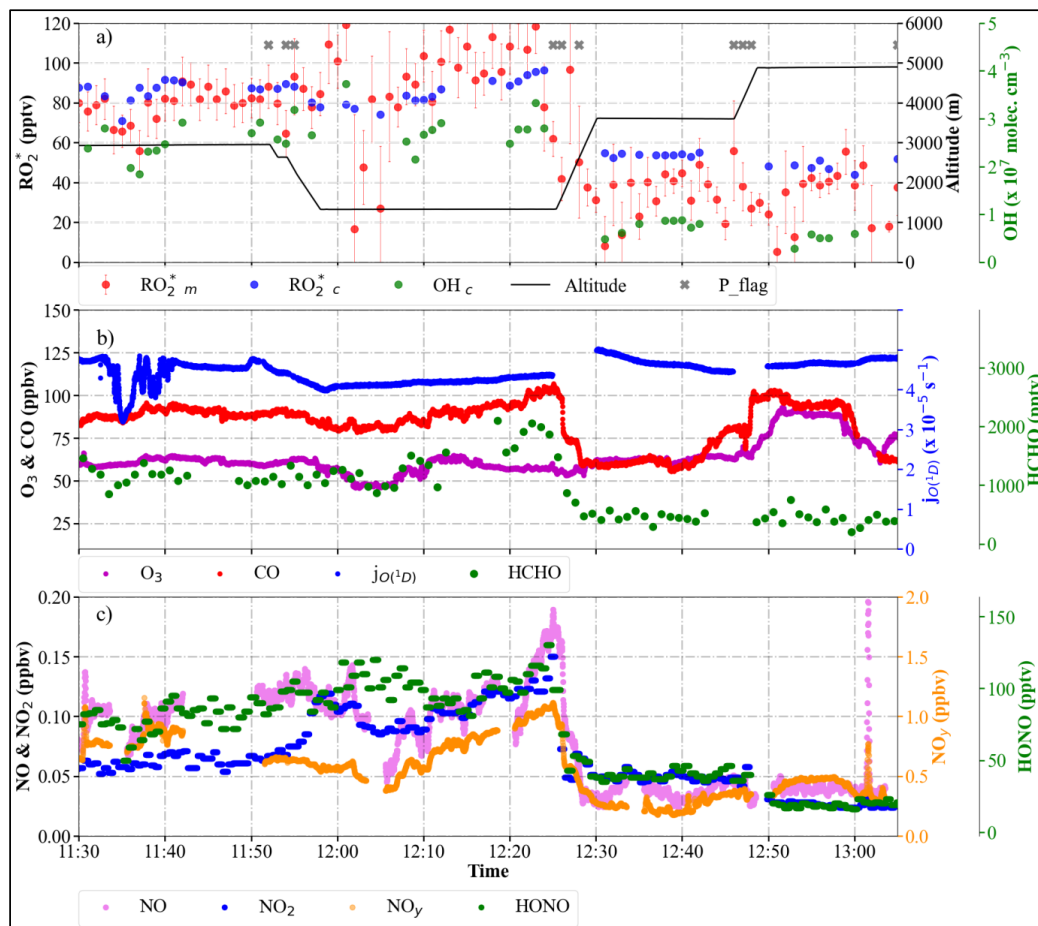
460 The applicability of Eq. 9 for calculating the in-flight measurements of RO_2^* along the track of the E-EU-03 flight on 11 July
461 2017 is shown in Fig. 16. The E-EU-03 flight investigated the outflow of selected MPCs in Italy (i.e., Po Valley and Rome).
462 Consequently, the flight track was routed along the western coast of Italy and included vertical profiling over the Tyrrhenian Sea
463 upwind of Rome (Fig. 15). As can be seen in $J_O(^1D)$, cloudless conditions dominated throughout the flight track. The $RO_2^* c$ agree
464 reasonably well with $RO_2^* m$ throughout this period except in the pollution plume measured from 12:05 to 12:25 UTC. In this
465 plume, CO, NO, NO_2 , HONO, NO_y , and HCHO reached 100 ppbv, 180 pptv, 150 pptv, 120 pptv, 1ppbv and 2 ppbv,
466 respectively. The RO_2^* measurements are approximately 20 % underestimated during this period. Backward trajectories
467 calculated using FLEXTRA indicate the transport of pollution through the Mediterranean mixed with dust plumes originating
468 from Tunisia. The NO mixing ratios observed indicate the proximity to emission sources.



469

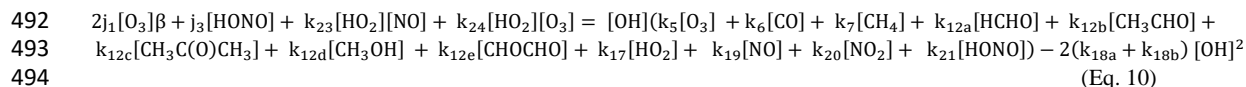
470 Figure 15: Maps of the flight track of E-EU-03 11 July 2017 along the western coast of Italy over the Tyrrhenian Sea colour-
471 coded with RO_2^* measurements.

472 The measurements of VOCs used in Eq. 9 may not be representative of the actual complex VOC composition in the plume
473 measured from 12:05 to 12:25 UTC. Consequently, the RO_2 to HO_2 ratio and the RO intermediates involved in the radical
474 interconversion processes, the branching ratios and effective rate coefficients for $\text{RO}_2^* - \text{RO}_2^*$ reactions might not be well
475 represented in Eq. 9. Taking CH_3O_2 as a surrogate for all RO_2 might lead to uncertainties in the RO_2^* calculations in the presence
476 of OVOCs with larger organic chains. On the experimental side, changes in the HO_2 to RO_2 ratio affect the accuracy of the
477 PerCEAS retrieval of the total sum of radicals. As noted in section 3, in this study $\text{RO}_2^* = \text{HO}_2 + 0.65 \times \text{RO}_2$, and the eCL is
478 determined for a 1:1 mixture of $\text{HO}_2:\text{CH}_3\text{O}_2$, i.e. $\delta = 0.5$ is used for the RO_2^* retrieval. However, the HO_2 to CH_3O_2 ratio is not
479 expected to remain constant in all the air masses probed. For a 3:1 ratio of $\text{HO}_2:\text{RO}_2$, the $\text{RO}_2^*_m$ would decrease by 10 %.
480 Similarly, a $\text{HO}_2:\text{RO}_2$ ratio of 1:3 would lead to an increase of 10 % in the reported $\text{RO}_2^*_m$. This uncertainty is well below the in-
481 flight uncertainty of the PerCEAS instrument indicated by the error bars in Fig. 16 (George et al., 2020), and cannot account for
482 the overall 20 % underestimations. However, it might reduce the differences observed between $\text{RO}_2^*_m$ and $\text{RO}_2^*_c$ in particular
483 cases. A complete explanation of the variability of RO_2^* in the pollution plumes measured within the IOP in Europe is beyond
484 the scope of this analysis and requires an investigation by high-resolution chemical models.



485
 486 Figure 16: Temporal variation of $RO_2^*_m$ and $RO_2^*_c$, selected radical precursors and $j_{O(^1D)}$ along the E-EU-03 flight track: a)
 487 $RO_2^*_m$, $RO_2^*_c$ and calculated OH (OH_c) mixing ratios. The flight altitude is indicated in black. The P_flag indicates RO_2^*
 488 measurements affected by dynamical pressure variation in the inlet; b) O_3 , CO, HCHO mixing ratios, and $j_{O(^1D)}$; c) NO, NO_2 ,
 489 NO_y , and HONO mixing ratios.

490 The OH concentrations in Fig. 16 are upper limits calculated by assuming pseudo-steady-state for the OH production (R1- R3,
 491 R24 and R26) and loss (R4 to R6, R13 and R15 to R19) reactions as described by Eq. 10:



495 The OH calculated from Eq. 10 assuming $\delta = 0.5$ is much higher than the OH concentration reported in the previous airborne
 496 (Crawfor et al., 1999; Tan et al. 2001) and ground-based measurements (Mihelcic et al., 2003; Kanaya et al., 2007, 2012;
 497 Hofzumahaus et al., 2009; Elshorbany et al., 2012; Lu et al., 2012, 2013; Tan et al., 2017, 2018; Whalley et al., 2018, 2021;
 498 Michelle et al., 2020) in different urban environments. This indicated that the limited number of OVOCs measurements available
 499 for the EMeRGe data set is insufficient to calculate the OH reactivity. The overestimation of OH agrees with the underestimation
 500 of $RO_2^*_m$ in air masses with a high amount of OVOCs ($\Sigma VOCS > 7$ ppbv) as the missing OH – OVOCs reactions in Eq. 8 should
 501 reduce ρ (the OH loss during the OH – RO_2^* interconversion) and thereby increase the $RO_2^*_c$. Due to the direct reaction of OH



502 with most of the gases emitted in the atmosphere, OH budget calculations in airmasses of complex chemistry are challenging and
503 require the experimental determination of the OH reactivity, as described by Tan et al. 2019 and Whalley et al., 2021.

504 4.4. Comparison of results with other studies

505 4.4.1 RO₂^{*} production rate

506 Cantrell et al. (2003b) proposed P_{RO₂^{*}} to be equal to the sum of two terms representing RO₂^{*} – RO₂^{*} reactions and the RO₂^{*} –
507 NO_x reactions in the troposphere. As a result of this assumption, the relationship between HO₂, RO₂, P_{RO₂^{*}} and NO_x is described
508 by Eq.11:

$$509 \quad P_{RO_2^*} = k_{RR} [HO_2 + RO_2]^2 + k_{RN} [HO_2 + RO_2] [NO_x] \quad (\text{Eq. 11})$$

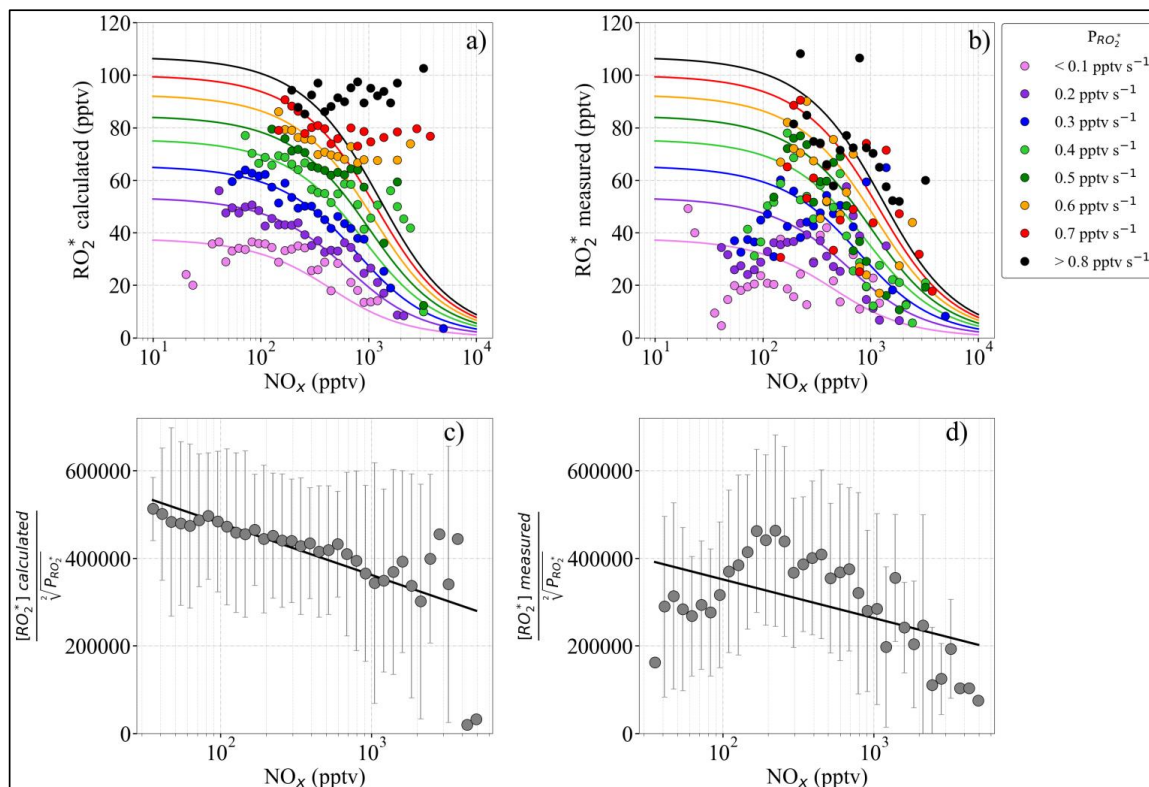
510 where k_{RR} and k_{RN} refer to effective rate coefficients for RO₂^{*} – RO₂^{*} and RO₂^{*} – NO_x reactions, and are calculated as fit
511 parameters. Solving Eq. 11 for [HO₂ + RO₂]² leads to:

$$512 \quad [HO_2 + RO_2] = \sqrt[3]{A + B^2} - B \quad (\text{Eq. 12})$$

513 where $A = \frac{P_{RO_2^*}}{k_{RR}}$ and $B = \frac{k_{RN}[NO_x]}{2 k_{RR}}$. For low NO_x and/or high P_{RO₂^{*}}, B becomes negligible compared to A. Then [HO₂ + RO₂]
514 approaches $\sqrt[3]{A}$ and is independent of NO_x. For high NO_x and /or low P_{RO₂^{*}}, [HO₂ + RO₂] approaches zero.

515 The least-square fitting in Eq. 12 is applied to RO₂^{*}_m and RO₂^{*}_c from the EMERGE measurements in Europe binned in 0.1 pptv s⁻¹
516 P_{RO₂^{*}} intervals as shown in Fig. 17. The fit parameters for Fig. 17a and Fig. 18b are k_{RR} = 7 × 10⁻⁵; k_{RN} = 9 × 10⁻⁶. The RO₂^{*}
517 calculated by Eq. 9 appears to be close to the linear function of the NO_x measured. Similar to the results of the study of Cantrell
518 et al. (2003b), a decrease of RO₂^{*} with NO_x is identified for NO_x > 1000 pptv, although only for P_{RO₂^{*}} < 0.7 pptv s⁻¹. In the study
519 of Cantrell et al. (2003b), P_{RO₂^{*}} only reached values up to 0.275 pptv s⁻¹.

520 Despite the low agreement of the fitted lines with the RO₂^{*}_m, a decrease of the RO₂^{*}_m as a function of NO_x is still observed. The
521 disagreement between the RO₂^{*}_m and the curves estimated using Eq. 12 implies that the simplified Eq. 11 is insufficient to
522 adequately describe the chemical and physical processes occurring in the troposphere. Part of the disagreement might arise from
523 missing terms in the P_{RO₂^{*}} calculation or inaccuracies related to the NO to NO₂ ratio in the air mass, which are more evident at
524 higher P_{RO₂^{*}}. As expected, the ratio of calculated [RO₂^{*}_c] to $\sqrt[3]{P_{RO_2^*}}$ has a negative linear dependency on the measured [NO_x] (see
525 Fig. 17c). The comparable plot of [RO₂^{*}_m] to $\sqrt[3]{P_{RO_2^*}}$ is not linear. This indicates that more complex non-linear processes are
526 involved in the air masses investigated than those considered in Eq. 11 (see Fig.17d).



527

528 Figure 17: a) $RO_2^*{}_c$ binned with $P_{RO_2^*}$; b) $RO_2^*{}_m$ binned with $P_{RO_2^*}$; c) $[RO_2^*]_c$ to $\sqrt{P_{RO_2^*}}$ ratio; and d) $[RO_2^*]_m$ to $\sqrt{P_{RO_2^*}}$ ratio. The
 529 data in a) and b) are coloured with radical production rates. The RO_2^* for different $P_{RO_2^*}$ ranges are binned into 50 bins over NO_x
 530 in the logarithmic scale from 10 to 10000 pptv. The solid lines are the least square fits obtained using Eq. 11. Error bars indicate
 531 $\pm 1\sigma$ of the bins.

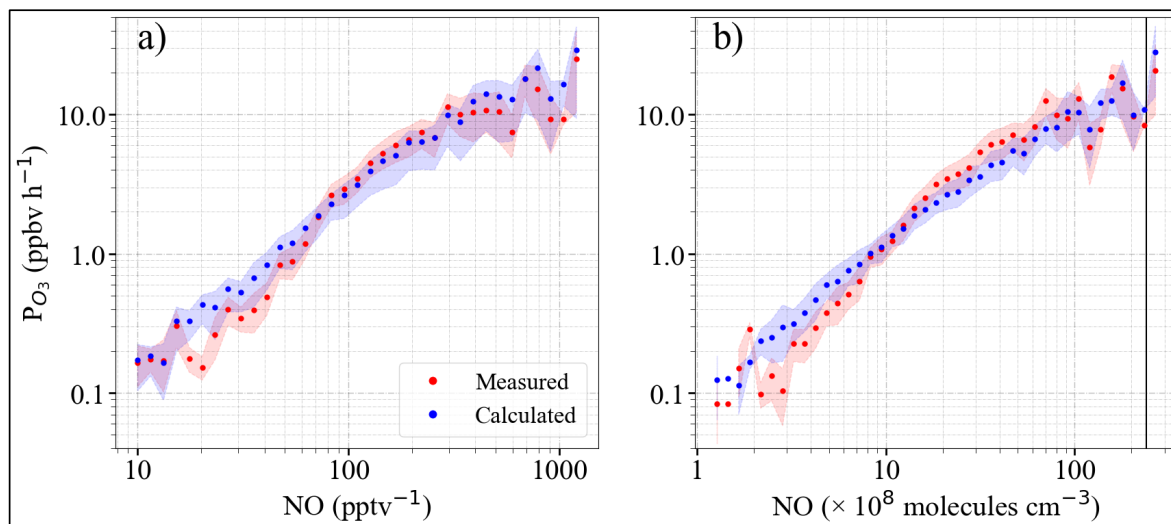
532 4.4.2 O_3 production rate

533 The O_3 production rate (P_{O_3}) is calculated from the EMeRGe Europe dataset using the reaction of RO_2^* with NO in a similar
 534 manner to that used in previous studies of photochemical processes in urban environments (e.g. Kleinman et al., 1995; Volz-
 535 Thomas et al., 2003; Mihelcic et al., 2003; Cantrell et al., 2003b; and references herein).

$$536 P_{O_3} = k_{RO_2^*+NO}[RO_2^*][NO] \quad (\text{Eq. 13})$$

537 where $k_{RO_2^*+NO}$ is taken as the average of k_{HO_2+NO} and $k_{CH_3O_2+NO}$.

538 Figure 18 shows plots of the mean P_{O_3} calculated using Eq. 13 from the $RO_2^*{}_m$ and $RO_2^*{}_c$ as a function of NO. The measurements
 539 are binned into 50 NO mixing ratio bins. The bin size increases with NO to keep the points equidistant in the logarithmic scale.
 540 The calculated P_{O_3} using the $RO_2^*{}_m$ and $RO_2^*{}_c$ agree well within the standard deviation of the bins.



541

542 Figure 18: Calculated P_{O_3} determined using $RO_2^*_m$ (red dots) and $RO_2^*_c$ (blue dots) as a function of: a) NO
543 mixing ratio; b) NO number concentration. The 1-minute measurements are binned into 50 bins over NO in the logarithmic scale
544 from 10 to 10000 pptv and from 5×10^7 to 3.5×10^{10} molecules cm^{-3} in 15a and 15b, respectively. The shaded area shows $\pm 1\sigma$
545 standard deviation of each bin. For comparison with ground-based measurements, the number concentration corresponding to 1
546 ppbv NO at 1000 mbar and 25°C has been marked by the solid black line in plot b).

547 Similar P_{O_3} values have been reported for ground-based measurements in polluted areas such as Wangdu (Tan et al., 2017) and
548 Beijing (Whalley et al., 2021) and similar ranges of peroxy radicals and NO mixing ratios. In previous work, Whalley et al.
549 (2018) calculated P_{O_3} to be about an order of magnitude lower than that found in this study from observations in central London
550 for about an order of magnitude lower amount of $HO_2 + RO_2$. For $NO > 1$ ppbv, the P_{O_3} estimated from the measurement of HO_2
551 and RO_2 , or from the assumptions of an HO_2 to RO_2 ratio were underestimated by the models in other studies in the urban
552 atmosphere (e.g. Martinez et al., 2003; Ren et al., 2003; Kanaya et al., 2008; Mao et al., 2010; Kanaya et al., 2012; Ren et al.,
553 2013; Brune et al., 2016; Griffith et al., 2016). This is generally attributed to underestimating large RO_2 concentrations, which
554 likely undergo multiple bimolecular reactions with NO before forming an HO_2 radical.

555 During the EMERGe IOP in Europe, the NO mixing ratios were < 1 ppbv (approximately $< 3 \times 10^{10}$ molecules cm^{-3}). The ozone
556 production rates obtained for both measured and calculated RO_2^* are in reasonable agreement with other modelling studies in
557 urban environments where the mixing ratio of NO is < 1 ppbv.

558 5. Summary and conclusions

559 This study exploits the airborne measurements of various atmospheric constituents on-board the HALO research aircraft over
560 Europe in summer 2017 to investigate radical photochemistry in the probed airmasses. RO_2^* are calculated by assuming a
561 photostationary steady-state (PSS) of RO_2^* and compared with the actual measurements. The calculation is constrained by the
562 simultaneous airborne measurements of radical precursors, photolysis frequencies and reactants of RO_2^* such as NO_x and O_3 .
563 The significance and the importance of selected production and loss processes in the RO_2^* chemistry are investigated by
564 gradually increasing the complexity of the analytical expression. The agreement of the calculations with the measurements over a
565 wide range of chemical composition and insolation conditions improves when the analytical expression is extended to account
566 for oxy-peroxy radical interconversion reactions and loss of OH and RO during the interconversion. The RO_2^* measured is



567 usually overestimated when NO is < 50 pptv in the air probed. This is attributed to RO₂^{*} loss processes involving reactions with
568 OH, which are not considered in the analytical expression. The reactions are excluded from the analytical expression to constrain
569 it with on-board measurements. These reactions become significant RO₂^{*} loss processes at low NO concentrations.

570 The results indicate that the steady-state calculations mostly underestimated the RO₂^{*} measurements in polluted plumes of urban
571 origin at altitudes below 2000 m. Changes in the HO₂ to RO₂ ratios in different plumes partly account for the disagreement in
572 particular cases. In pollution plumes with the sum of the OVOCs measured mixing ratios > 7 ppbv, the underestimation of the
573 measurements can reach up to 80 %. In these plumes, the oxidation and/or photolysis of non-measured VOCs and the ozonolysis
574 of alkenes might be significant, limiting the accuracy of the analytical expression. The overestimation of the OH concentration
575 calculated based on the measured reactants also indicates missing oxy-peroxy radical interconversion reactions in the analytical
576 PSS expression. More information about peroxy radical speciation and VOC partitioning is required to better describe the fast
577 photochemistry in these pollution plumes.

578 The analytical expression developed is robust enough to simulate the radical chemistry in most of the conditions in the free
579 troposphere encountered during EMERGe IOP in Europe. Speciated radical and VOC measurements in future campaigns would
580 facilitate the estimation of radical loss reactions in air masses with NO < 50 pptv and improve radical production rates
581 estimations in pollution plumes with a high amount of VOCs, where non-linear complex chemistry is involved. Comparing RO₂^{*}
582 measurements with RO₂^{*} calculations from the analytical expression helps to identify different chemical and physical regimes,
583 which can be used to constrain future model studies.

584 The calculated O₃ production rates for NO < 1 ppbv are in the same order of magnitude as those previously reported for urban
585 environments. This indicates that the selected RO₂^{*} production and loss processes and observations of the radical precursors on-
586 board are, to a good approximation, adequate for the estimation of the O₃ production in the measured airmasses in the free
587 troposphere over Europe.

588 *Competing interests.* The authors declare that they have no conflict of interest.

589
590 *Financial support.* The study was funded in part by the German Research Foundation (Deutsche Forschungsgemeinschaft; DFG)
591 HALO-SPP 1294, the University and the State of Bremen, IPA, DLR, Oberpfaffenhofen, Germany. The contributions from BS, FK, and KP
592 were supported via the DFG grants PF 384/16, PF 384/17 and PF 384/19. KB was granted funding via the DFG grant PI 193/21-1 and
593 acknowledges additional financial from the Heidelberg Graduate School for Physics. EF was supported via the DFG grant NE 2150/1-1 and
594 acknowledges additional financial support from the Karlsruhe Institute of Technology. MG, YL, MDAH and JPB acknowledge financial
595 support from the University of Bremen.

596 **Acknowledgements:**

597 MG, MDAH, YL and JPB thank Wilke Thomssen for support during the preparation and integration phases of EMERGe.

598 **Author contribution:**

599 MG, VN, and YL undertook the RO₂^{*} measurements, flying as key scientists on-board HALO. VN led the deployment of
600 PeRCEAS in the HALO aircraft. MG led the analysis of the PeCEAS measurements and prepared the manuscript with
601 contributions from all co-authors. MDAH and JPB initiated the EMERGe research project and consortium, acted as co-principal
602 and principal investigators, and participated in the measurement campaigns. They developed the overarching EMERGe scientific
603 objectives and the required measurement portfolio, directed the EMERGe research campaigns, and participated in the data



604 analysis presented. AZ, BB, BS, EF, FO, FK, HS, HZ, KB, KP, and TH have contributed by providing their measurements made
605 on-board HALO during the campaign and participated in the discussion of results.

606 **Competing interests:**

607 The authors declare that they have no conflict of interest.

608 **6. References**

609 Andreae, M. O. , Afchine, A. Albrecht, R., Holanda, B. A., Artaxo, P., Barbosa, H. M. J., Borrmann, S., Cecchini, M. A., Costa,
610 A., Dollner, M., Fütterer, D., Järvinen, E., Jurkat, T., Klimach, T., Konemann, T., Knote, C., Krämer, M., Krisna, T., Machado,
611 L. A. T., Mertes, S.; Minikin, A. , Pöhlker, C., Pöhlker, M. L., Pöschl, U. Rosenfeld, D., Sauer, D., Schlager, H., Schnaiter, M.,
612 Schneider, J., Schulz, C., Spanu, A., Sperling, V. B., Voigt, C., Walser, A., Wang, J., Weinzierl, B., Wendisch, M. , Ziereis, H.:
613 Aerosol characteristics and particle production in the upper troposphere over the Amazon Basin. *Atmos. Chem. Phys.*, 18, 921–
614 961, <https://doi.org/10.5194/acp-18-921-2018>, 2018.

615 Andrés-Hernández, M. D., Kartal, D., Reichert, L., Burrows, J. P., Meyer Arnek, J., Lichtenstern, M., Stock, P., and Schlager,
616 H.: Peroxy radical observations over West Africa during AMMA 2006: photochemical activity in the outflow of convective
617 systems, *Atmos. Chem. Phys.*, 9, 3681–3695, <https://doi.org/10.5194/acp-9-3681-2009>, 2009.

618 Andrés Hernández, M. D., Hilboll, A., Ziereis, H., Förster, E., Krüger, O. O., Kaiser, K., Schneider, J., Barnaba, F., Vrekoussis,
619 M., Schmidt, J., Huntrieser, H., Blechschmidt, A.-M., George, M., Nenakhov, V., Klausner, T., Holanda, B. A., Wolf, J.,
620 Eirenschmalz, L., Krebsbach, M., Pöhlker, M. L., Hedegaard, A. B., Mei, L., Pfeilsticker, K., Liu, Y., Koppmann, R., Schlager,
621 H., Bohn, B., Schumann, U., Richter, A., Schreiner, B., Sauer, D., Baumann, R., Mertens, M., Jöckel, P., Kilian, M., Stratmann,
622 G., Pöhlker, C., Campanelli, M., Pandolfi, M., Sicard, M., Gomez-Amo, J. L., Pujadas, M., Bigge, K., Kluge, F., Schwarz, A.,
623 Daskalakis, N., Walter, D., Zahn, A., Pöschl, U., Bönisch, H., Borrmann, S., Platt, U., and Burrows, J. P.: Overview: On the
624 transport and transformation of pollutants in the outflow of major population centres – observational data from the EMERGE
625 European intensive operational period in summer 2017, *Atmos. Chem. Phys. Discuss.* [preprint], [https://doi.org/10.5194/acp-](https://doi.org/10.5194/acp-2021-500)
626 2021-500, in review, 2021.

627 Brito, J., and Zahn, A.: An unheated permeation device for calibrating atmospheric VOC measurements, *Atmos. Meas. Tech.*,
628 4(10), 2143–2152, <https://doi.org/10.5194/amt-4-2143-2011>, 2011.

629 Brune, W. H., Baier, B. C., Thomas, J., Ren, X., Cohen, R. C., Pusede, S. E., Browne, E. C., Goldstein, A. H., Gentner, D. R.,
630 Keutsch, F. N., Thornton, J. A., Harrold, S., Lopez-Hilfiker, F. D., and Wennberg, P. O.: Ozone production chemistry in the
631 presence of urban plumes, *Faraday Discuss.*, 189, 169–189, <https://doi.org/10.1039/c5fd00204d>, 2016.

632 Burkholder, J. B., Sander, S. P., Abbatt, J., Barker, J. R., Huie, R. E., Kolb, C. E., Kurylo, M. J., Orkin, V. L. Wilmouth, D. M.,
633 and Wine P. H.: Chemical Kinetics and Photochemical Data for Use in Atmospheric Studies, Evaluation No. 18, JPL Publication
634 15-10, Jet Propulsion Laboratory, Pasadena, available at: <http://jpldataeval.jpl.nasa.gov> (last access: 7 April 2020), 2015.

635 Cantrell, C. A. and Stedman, D. H.: A possible technique for the measurement of atmospheric peroxy radicals, *Geophys. Res.*
636 *Let.*, 9, 846–849, 1982.



- 637 Cantrell, C. A., Stedman, D. H., and Wendel, G. J.: Measurement of atmospheric peroxy radicals by chemical amplification,
638 *Anal. Chem.*, 56, 1496–1502, 1984
- 639 Cantrell, C. A., Shetter, R. E., Calvert, J. G., Eisele, F. L., Williams, E., Baumann, K., Brune, W. H., Stevens, P. S., Mather J. H.:
640 Peroxy radicals from photostationary state deviations and steady state calculations during the Tropospheric OH Photochemistry
641 Experiment at Idaho Hill, Colorado, 1993, *J. Geophys. Res.*, 102(D5), 6369, [https://doi.org/](https://doi.org/10.1029/96JD01703) <https://doi.org/10.1029/96JD01703>,
642 1997.
- 643 Cantrell, C. A., G. D. Edwards, S. Stephens, L. Mauldin, E. Kosciuch, M. Zondlo, and F. Eisele.: Peroxy radical observations
644 using chemical ionisation mass spectrometry during TOPSE, *J. Geophys. Res.*, 108(D6), 8381,
645 <https://doi.org/10.1029/2002JD002715>, 2003a.
- 646 Cantrell, C. A., Edwards, G. D., Stephens, S., Mauldin, R.L., Zondlo, M.A., Kosciuch, E., Eisele, F. L., Shetter, R. E., Lefer, B.
647 L., Hall, S., Flocke, F., Weinheimer, A., Fried, A., Apel, E., Kondo, Y., Blake, D. R., Blake, N. J., Simpson, I. J., Bandy, A. R.,
648 Thornton, D. C., Heikes, B. G., Singh, H. B., Brune, W. H., Harder, H., Martinez, M., Jacob, D. J., Avery, M. A., Barrick, J. D.,
649 Sachse, G. W., Olson, J. R., Crawford, J. H., and Clarke, A. D.: Peroxy radical behaviour during the Transport and Chemical
650 Evolution over the Pacific (TRACE-P) campaign as measured aboard the NASA -3B aircraft, *J. Geophys. Res.*, 108(D20), 8797,
651 <https://doi.org/10.1029/2003JD003674>, 2003b.
- 652 Chen H., Winderlich, J., Gerbig, C., Hofer, A., Rella, C. W., Crosson, E. R., Van Pelt, A. D., Steinbach, J., Kolle, O., Beck, V.,
653 Daube, B. C., Gottlieb, E. W., Chow, V. Y., Santoni, G. W., and S. C. Wofsy, High-accuracy continuous airborne measurements
654 of greenhouse gases (CO₂ and CH₄) using the cavity ring-down spectroscopy (CRDS) technique, *Atmos. Mes. Tech.*, 3, 375-
655 386, 2010.
- 656 Crawford, J., Davis, D., Olson, J., Chen, G., Liu, S., Gregory, G., Barrick, J., Sachse, G., Sandholm, S., Heikes, B., Singh, H.,
657 and Blake, D.: Assessment of upper tropospheric HO_x sources over the tropical Pacific based on NASA GTE/PEM data: Net
658 effect on HO_x and other photochemical parameters, *J. Geophys. Res.*, 104, 16255–16273,
659 <https://doi.org/10.1029/1999JD900106>, 1999.
- 660 Elshorbany, Y. F., Kleffmann, J., Hofzumahaus, A., Kurtenbach, R., Wiesen, P., Brauers, T., Bohn, B., Dorn, H.-P., Fuchs, H.,
661 Holland, F., Rohrer, F., Tillmann, R., Wegener, R., Wahner, A., Kanaya, Y., Yoshino, A., Nishida, S., Kajii, Y., Martinez, M.
662 Kubistin, D., Harder, H., Lelieveld, J., Elste, T., Plass-Dülmer, C., Stange, G., Berresheim, H., Schurath, U.: HO_x budgets
663 during HO_xComp: A case study of HO_x chemistry under NO_x-limited conditions, *J. Geophys. Res.*, 117, D03307,
664 <https://doi.org/10.1029/2011JD017008>.
- 665 Fisher, R., Lowry, D., Wilkin, O., Sriskantharajah, S., and Nisbet, E. G.: High-precision, automated stable isotope analysis of
666 atmospheric methane and carbon dioxide using continuous-flow isotope-ratio mass spectrometry, *Rapid communications in mass*
667 *spectrometry: RCM*, 20 (2), 200–208. <https://doi.org/10.1002/rcm.2300>, 2006.
- 668 Fricke, C., Ehrlich, A., Jäkel, E., Bohn, B., Wirth, M., and Wendisch, M.: Influence of local surface albedo variability and ice
669 crystal shape on passive remote sensing of thin cirrus, *Atmos. Chem. Phys.*, 14, 1943–1958, [https://doi.org/10.5194/acp-14-1943-](https://doi.org/10.5194/acp-14-1943-2014)
670 2014, 2014.



- 671 General, S., Pöhler, D., Sihler, H., Bobrowski, N., Frieß, U., Zielcke, J., Horbanski, M., Shepson, P. B., Stirm, B. H., Simpson,
672 W. R., Weber, K., Fischer, C., and Platt, U.: The Heidelberg Airborne Imaging DOAS Instrument (HAIDI) – a novel Imaging
673 DOAS device for 2-D and 3-D imaging of trace gases and aerosols, *Atmos. Meas. Tech.*, *7*, 3459–3485, 2014,
674 <https://doi.org/10.5194/amt-7-3459-2014>.
- 675 George, M., Andrés-Hernández, M. D., Nenakhov, V., Liu, Y., and Burrows, J. P.: Airborne measurement of peroxy radicals
676 using chemical amplification coupled with cavity ring-down spectroscopy: the PerCEAS instrument, *Atmos. Meas. Tech.* *13*,
677 2577–2600, <https://doi.org/10.5194/amt-13-2577-2020>.
- 678 Gerbig, C., Kley, D., Volz-Thomas, A., Kent, J., Dewey, K., and McKenna, D. S.: Fast response resonance fluorescence CO
679 measurements aboard the C-130: Instrument characterisation and measurements made during North Atlantic Regional
680 Experiment 1993, *J. Geophys. Res.*, *101*, 29229–29238, 1996.
- 681 Griffith, S. M., Hansen, R. F., Dusanter, S., Michoud, V., Gilman, J. B., Kuster, W. C., Veres, P. R., Graus, M., de Gouw, J. A.,
682 Roberts, J., Young, C., Washenfelder, R., Brown, S. S., Thalman, R., Waxman, E., Volkamer, R., Tsai, C., Stutz, J., Flynn, J. H.,
683 Grossberg, N., Lefer, B., Alvarez, S. L., Rappenglueck, B., Mielke, L. H., Osthoff, H. D., and Stevens, P. S.: Measurements of
684 Hydroxyl and Hydroperoxy Radicals during CalNexLA: Model Comparisons and Radical Budgets, *J. Geophys. Res.-Atmos.*,
685 *121*, 4211–4232, <https://doi.org/10.1002/2015JD024358>, 2016.
- 686 Hofzumahaus, A., Rohrer, F., Lu, K., Bohn, B., Brauers, T., Chang, C.-C., Fuchs, H., Holland, F., Kita, K., Kondo, Y., Li, X.,
687 Lou, S., Shao, M., Zeng, L., Wahner, A., and Zhang, Y.: Amplified trace gas removal in the troposphere, *Science*, *324*, 1702–
688 1704, <https://doi.org/10.1126/science.1164566>, 2009.
- 689 Horstjann, M., Andrés Hernández, M. D., Nenakhov, V., Chrobry, A., and Burrows, J. P.: Peroxy radical detection for airborne
690 atmospheric measurements using absorption spectroscopy of NO₂, *Atmos. Meas. Tech.* *7*, 1245–1257, <https://doi.org/10.5194/amt-7-1245-2014>.
- 692 Hüneke, T., Aderhold, O.-A., Bounin, J., Dorf, M., Gentry, E., Grossmann, K., Groß, J.-U., Hoor, P., Jöckel, P., Kenntner, M.,
693 Knapp, M., Knecht, M., Lörks, D., Ludmann, S., Matthes, S., Raecke, R., Reichert, M., Weimar, J., Werner, B., Zahn, A.,
694 Ziereis, H., and Pfeilsticker, K.: The novel HALO mini-DOAS instrument: inferring trace gas concentrations from airborne
695 UV/visible limb spectroscopy under all skies using the scaling method, *Atmos. Meas. Tech.*, *10*, 4209–4234,
696 <https://doi.org/10.5194/amt-10-4209-2017>, 2017.
- 697 Inomata, S., Tanimoto, H., Kameyama, S., Tsunogai, U., Irie, H., Kanaya, Y., and Wang, Z.: Technical Note: Determination of
698 formaldehyde mixing ratios in air with PTR-MS: laboratory experiments and field measurements, *Atmos. Chem. Phys.*, *8*, 273–
699 284, <https://doi.org/10.5194/acp-8-273-2008>, 2008.
- 700 Kanaya, Y., Cao, R., Akimoto, H., Fukuda, M., Komazaki, Y., Yokouchi, Y., Koike, M., Tanimoto, H., Takegawa, N., and
701 Kondo, Y.: Urban photochemistry in central Tokyo: 1. Observed and modelled OH and HO₂ radical concentrations during the
702 winter and summer of 2004, *J. Geophys. Res.*, *112*, D21312, <https://doi.org/10.1029/2007JD008670>, 2007.



- 703 Kanaya, Y., Fukuda, M., Akimoto, H., Takegawa, N., Komazaki, Y., Yokouchi, Y., Koike, M., and Kondo, Y.: Urban
704 photochemistry in central Tokyo: 2. Rates and regimes of oxidant (O₃ + NO₂) production, *J. Geophys. Res.*, 113, D06301,
705 <https://doi.org/10.1029/2007JD008671>, 2008.
- 706 Kanaya, Y., Hofzumahaus, A., Dorn, H.-P., Brauers, T., Fuchs, H., Holland, F., Rohrer, F., Bohn, B., Tillmann, R., Wegener, R.,
707 Wahner, A., Kajii, Y., Miyamoto, K., Nishida, S., Watanabe, K., Yoshino, A., Kubistin, D., Martinez, M., Rudolf, M., Harder,
708 H., Berresheim, H., Elste, T., Plass-Dülmer, C., Stange, G., Kleffmann, J., Elshorbany, Y., and Schurath, U.: Comparisons of
709 observed and modeled OH and HO₂ concentrations during the ambient measurement period of the HOxComp field campaign,
710 *Atmos. Chem. Phys.*, 12, 2567–2585, <https://doi.org/10.5194/acp-12-2567-2012>, 2012.
- 711 Kartal, D., Andrés-Hernández, M. D., Reichert, L., Schlager, H., and Burrows, J. P.: Technical Note: Characterisation of a
712 DUALER instrument for the airborne measurement of peroxy radicals during AMMA 2006, *Atmos. Chem. Phys.*, 10, 3047–
713 3062, <https://doi.org/10.5194/acp-10-3047-2010>, 2010.
- 714 Kleinman, L., Y.-N. Lee, S. R. Springston, J. H. Lee, L. Nunnermacker, J. Weinstein-Lloyd, X. Zhou, and L. Newman, Peroxy
715 radical concentration and ozone formation rate at a rural site in southeastern United States, *J. Geophys. Res.*, 100, 7263– 7273,
716 1995.
- 717 Kluge, F., Hüneke, T., Knecht, M., Lichtenstern, M., Rotermund, M., Schlager, H., Schreiner, B., and Pfeilsticker, K.: Profiling
718 of formaldehyde, glyoxal, methylglyoxal, and CO over the Amazon: normalized excess mixing ratios and related emission
719 factors in biomass burning plumes, *Atmos. Chem. Phys.*, 20, 12363–12389, <https://doi.org/10.5194/acp-20-12363-2020>, 2020.
- 720 Lew, M. M., Rickly, P. S., Bottorff, B. P., Reidy, E., Sklaveniti, S., Léonardis, T., Locoge, N., Dusanter, S., Kundu, S., Wood,
721 E., and Stevens, P. S.: OH and HO₂ radical chemistry in a midlatitude forest: measurements and model comparisons, *Atmos.*
722 *Chem. Phys.*, 20, 9209–9230, <https://doi.org/10.5194/acp-20-9209-2020>, 2020.
- 723 Lu, K. D., Rohrer, F., Holland, F., Fuchs, H., Bohn, B., Brauers, T., Chang, C. C., Häsel, R., Hu, M., Kita, K., Kondo, Y., Li,
724 X., Lou, S. R., Nehr, S., Shao, M., Zeng, L. M., Wahner, A., Zhang, Y. H., and Hofzumahaus, A.: Observation and modelling of
725 OH and HO₂ concentrations in the Pearl River Delta 2006: a missing OH source in a VOC rich atmosphere, *Atmos. Chem.*
726 *Phys.*, 12, 1541–1569, <https://doi.org/10.5194/acp-12-1541-2012>, 2012.
- 727 Lu, K. D., Hofzumahaus, A., Holland, F., Bohn, B., Brauers, T., Fuchs, H., Hu, M., Häsel, R., Kita, K., Kondo, Y., Li, X., Lou,
728 S. R., Oebel, A., Shao, M., Zeng, L. M., Wahner, A., Zhu, T., Zhang, Y. H., and Rohrer, F.: Missing OH source in a suburban
729 environment near Beijing: observed and modelled OH and HO₂ concentrations in summer 2006, *Atmos. Chem. Phys.*, 13, 1057–
730 1080, <https://doi.org/10.5194/acp-13-1057-2013>, 2013.
- 731 Mallaun, C., Giez, A. and Baumann, R.: Calibration of 3-D wind measurements on a single engine research aircraft *Atmos.*
732 *Meas. Tech.*, 8, 3177–3196, <https://doi.org/10.5194/amt-8-3177-2015>, 2015.
- 733 Mihelcic, D., Holland, F., Hofzumahaus, A., Hoppe, L., Konrad, S., Müsgen, P., Pätz, H.-W., Schäfer, H.-J., Schmitz, T., Volz-
734 Thomas, A., Bächmann, K., Schlösmki, S., Platt, U., Geyer, A., Alicke, B., and Moortga, G. K.: Peroxy radicals during
735 BERLIOZ at Pabstthum: Measurements, radical budgets and ozone production, *J. Geophys. Res.*, 108, 8254,
736 <https://doi.org/10.1029/2001JD001014>, 2003.



- 737 Mao, J., Jacob, D. J., Evans, M. J., Olson, J. R., Ren, X., Brune, W. H., Clair, J. M. St., Crouse, J. D., Spencer, K. M., Beaver,
738 M. R., Wennberg, P. O., Cubison, M. J., Jimenez, J. L., Fried, A., Weibring, P., Walega, J. G., Hall, S. R., Weinheimer, A. J.,
739 Cohen, R. C., Chen, G., Crawford, J. H., McNaughton, C., Clarke, A. D., Jaeglé, L., Fisher, J. A., Yantosca, R. M., Le Sager, P.,
740 and Carouge, C.: Chemistry of hydrogen oxide radicals (HOx) in the Arctic troposphere in spring, *Atmos. Chem. Phys.*, 10,
741 5823– 5838, <https://doi.org/10.5194/acp-10-5823-2010>, 2010.
- 742 Ren, X., Harder, H., Martinez, M., Leshner, R. L., Oligier, A., Shirley, T., Adams, J., Simpas, J. B., and Brune, W. H.: HOX
743 concentrations and OH reactivity observations in New York City during PMTACS-NY2001, *Atmos. Environ.*, 37, 3627–3637,
744 2003.
- 745 Ren, X., van Duin, D., Cazorla, M., Chen, S., Mao, J., Zhang, L., Brune, W. H., Flynn, J. H., Grossberg, N., Lefer, B. L.,
746 Rappenglück, B., Wong, K. W., Tsai, C., Stutz, J., Dibb, J. E., Thomas Jobson, B., Luke, W. T., and Kelley, P.: Atmospheric
747 oxidation chemistry and ozone production: Results from SHARP 2009 in Houston, Texas, *J. Geophys. Res.*, 118, 5770–5780,
748 <https://doi.org/10.1002/jgrd.50342>, 2013.
- 749 Ren, Y., Baumann, R., Schlager, H.: An airborne perfluorocarbon tracer system and its first application for a Lagrangian
750 experiment. *Atmos. Meas. Tech.*, 8, 69-80. <https://doi.org/10.5194/amt-8-69-2015>, 2015.
- 751 Ridley, B.A., Madronich, S., Chatfield, R. B., Walega, J. G., and Shetter, R. E.: Measurements and model simulations of the
752 photostationary state during the Mauna Loa observatory photochemistry experiment: Implications for radical concentrations and
753 ozone production and loss rates, *J. Geophys. Res.* 97, 10375-10388 (1992).
- 754 Rotermund, M. K., Bense, V., Chipperfield, M. P., Engel, A., Groß, J.-U., Hoor, P., Hüneke, T., Keber, T., Kluge, F., Schreiner,
755 B., Schuck, T., Vogel, B., Zahn, A., and Pfeilsticker, K.: Organic and inorganic bromine measurements around the extratropical
756 tropopause and lowermost stratosphere: Insights into the transport pathways and total bromine, *Atmos. Chem. Phys. Discuss.*
757 [preprint], <https://doi.org/10.5194/acp-2021-202>, in review, 2021.
- 758 Stutz, J., Werner, B., Spolaor, M., Scalone, L., Festa, J., Tsai, C., Cheung, R., Colosimo, S. F., Tricoli, U., Raecke, R., Hossaini,
759 R., Chipperfield, M. P., Feng, W., Gao, R.-S., Hints, E. J., Elkins, J. W., Moore, F. L., Daube, B., Pittman, J., Wofsy, S.,
760 and Pfeilsticker, K.: A new Differential Optical Absorption Spectroscopy instrument to study atmospheric chemistry from a
761 high-altitude unmanned aircraft, *Atmos. Meas. Tech.*, 10, 1017 – 1042, <https://doi.org/10.5194/amt-10-1017-2017>, 2017.
- 762 Schulz, C., Schneider, J., Holanda, B. A., Appel, O., Costa, A., de Sá, S.S., Dreiling, V., Fütterer, D., Jurkat-Witschas, T.,
763 Klimach, T., Knöbe, C., Krämer, M., Martin, S.T., Mertes, S., Pöhlker, M.L., Sauer, D., Voigt, C., Walser, A., Weinzierl, A.B.,
764 Ziereis, H., Zöger, M., Andreae, M.O., Artaxo, P., Machado, L.-A.T., Pöschl, U., Wendisch, M., and S. Borrmann, Aircraft-based
765 observations of isoprene-epoxydiol-derived secondary organic aerosol (IEPOX-SOA) in the tropical upper troposphere over the
766 Amazon region. *Atmos. Chem. Phys.*, 18, 14979–15001, 2018, <https://doi.org/10.5194/acp-18-14979-2018>.
- 767 Schumann, U.: Measurement and model data comparisons for the HALO-FAAM formation flight during EMERGE on 17 July
768 2017, doi:10.5281/zenodo.4427965, 2020.



- 769 Speidel, M., Nau, R., Arnold, F., Schlager, H., A. Stohl, Sulfur dioxide measurements in the lower, middle and upper
770 troposphere: Deployment of an aircraft-based chemical ionisation mass spectrometer with permanent in-flight calibration,
771 *Atmospheric Environment*, 41, 2427-2437, <https://doi.org/10.1016/j.atmosenv.2006.07.047>, 2007.
- 772 Tan, D., Faloon, I., Simpas, J. B., Brune, W., Olson, J., Crawford, J., Avery, M., Sachse, G., Vay, S., Sandholm, S., Guan, H.-
773 W., Vaughn, T., Mastromarino, J., Heikes, B., Snow, J., Podolske, J., and Singh, H.: OH and HO₂ in the tropical Pacific: Results
774 from PEMTropics B, *J. Geophys. Res.*, 106, 32,667–32,681, 2001.
- 775 Tan, Z., Fuchs, H., Lu, K., Hofzumahaus, A., Bohn, B., Broch, S., Dong, H., Gomm, S., Häsel, R., He, L., Holland, F., Li, X.,
776 Liu, Y., Lu, S., Rohrer, F., Shao, M., Wang, B., Wang, M., Wu, Y., Zeng, L., Zhang, Y., Wahner, A., and Zhang, Y.: Radical
777 chemistry at a rural site (Wangdu) in the North China Plain: observation and model calculations of OH, HO₂ and RO₂ radicals,
778 *Atmos. Chem. Phys.*, 17, 663–690, <https://doi.org/10.5194/acp-17-663-2017>, 2017.
- 779 Tan, Z., Rohrer, F., Lu, K., Ma, X., Bohn, B., Broch, S., Dong, H., Fuchs, H., Gkatzelis, G. I., Hofzumahaus, A., Holland, F., Li,
780 X., Liu, Y., Liu, Y., Novelli, A., Shao, M., Wang, H., Wu, Y., Zeng, L., Hu, M., Kiendler-Scharr, A., Wahner, A., and Zhang,
781 Y.: Wintertime photochemistry in Beijing: observations of RO_x radical concentrations in the North China Plain during the
782 BEST-ONE campaign, *Atmos. Chem. Phys.*, 18, 12391–12411, <https://doi.org/10.5194/acp-18-12391-2018>, 2018.
- 783 Tyndall, G. S.; Cox, R. A.; Granier, C.; Lesclaux, R.; Moortgat, G. K.; Pilling, M. J.; Ravishankara, A. R.; Wallington, T. J.
784 Atmospheric chemistry of small organic peroxy radicals. *J. Geophys. Res.* 2001, 106, 12157-12182,
785 <https://doi.org/10.1029/2000JD900746>.
- 786 Volz-Thomas, A., Xueref, I., and Schmitt, R.: Automatic gas chromatograph and calibration system for ambient measurements
787 of PAN and PPN, *Environ. Sci. Poll. Res.*, 9, 72-76, 2001.
- 788 Volz-Thomas, A., Pätz, H - W., Houben, N., Konrad, S., Mihelcic, D., Klüpfel, T., Perner, D.: Inorganic trace gases and peroxy
789 radicals during BERLIOZ at Pabstthum: An investigation of the photostationary state of NO_x and O₃, *J. Geophys. Res.*, 108(D4),
790 PHO 4-1, <https://doi.org/10.1029/2001JD001255>, 2003.
- 791 Wendisch, M., Pöschl, U., Andreae, M. O., Machado, L. A. T., Albrecht, R., Schlager, H., Rosenfeld, D., Martin, S. T.,
792 Abdelmonem, A. Afchine, A., Araújo, A. C., Artaxo, P., Aufmhoff, H., Barbosa, H. M. J., Borrmann, S., Braga, R., Buchholz,
793 B., Cecchini, M. A., Costa, A. Curtius, J., Dollner, M., Dorf, M., Dreiling, V., Ebert, V., Ehrlich, A., Ewald, F., Fisch, G., Fix,
794 A., Frank, F., Fütterer, D., Heckl, C., Heidelberg, F., Hüneke, T., Jäkel, E., Järvinen, E., Jurkat, T., Kanter, S., Kästner, U.,
795 Kenntner, M., Kesselmeier, J., Klimach, T., Knecht, M., Kohl, R., Kölling, T., Krämer, M., Krüger, M., Krisna, T. C., Lavric, J.
796 V., Longo, K., Mahnke, C., Manzi, A. O., Mayer, B., Mertes, S., Minikin, A., Molleker, S., Münch, S., Nillius, B., Pfeilsticker,
797 K., Pöhlker, C., Roiger, A., Rose, D., Rosenow, D., Sauer, D., Schnaiter, M., Schneider, J., Schulz, C., de Souza, R. A. F. Spanu,
798 A., Stock, P., Vila, D., Voigt, C., Walser, A., Walter, D., Weigel, R., Weinzierl, B., Werner, F., Yamasoe, M. A., Ziereis, H.,
799 Zinner, T., and Zöger, M.: The ACRIDICON-CHUVA campaign: Studying tropical deep convective clouds and precipitation
800 over Amazonia using the new German research aircraft HALO, *Bull. Amer. Meteorol. Soc.*, 97, 1885-1908, <https://doi.org/10.1175/BAMS-D-14-00255>, 2016.



- 802 Whalley, L. K., Stone, D., Dunmore, R., Hamilton, J., Hopkins, J. R., Lee, J. D., Lewis, A. C., Williams, P., Kleffmann, J.,
803 Laufs, S., Woodward-Massey, R., and Heard, D. E.: Understanding in situ ozone production in the summertime through radical
804 observations and modelling studies during the Clean air for London project (ClearfLo), *Atmos. Chem. Phys.*, 18, 2547–2571,
805 <https://doi.org/10.5194/acp-18-2547-2018>, 2018.
- 806 Whalley, L. K., Slater, E. J., Woodward-Massey, R., Ye, C., Lee, J. D., Squires, F., Hopkins, J. R., Dunmore, R. E., Shaw, M.,
807 Hamilton, J. F., Lewis, A. C., Mehra, A., Worrall, S. D., Bacak, A., Bannan, T. J., Coe, H., Percival, C. J., Ouyang, B., Jones, R.
808 L., Crilley, L. R., Kramer, L. J., Bloss, W. J., Vu, T., Kotthaus, S., Grimmond, S., Sun, Y., Xu, W., Yue, S., Ren, L., Acton, W.
809 J. F., Hewitt, C. N., Wang, X., Fu, P., and Heard, D. E.: Evaluating the sensitivity of radical chemistry and ozone formation to
810 ambient VOCs and NO_x in Beijing, *Atmos. Chem. Phys.*, 21, 2125–2147, <https://doi.org/10.5194/acp-21-2125-2021>, 2021.
- 811 Wintel, J., Hösen, E., Koppmann, R., Krebsbach, M., Hofzumahaus, A., and Rohrer, F.: Stable carbon isotope ratios of toluene in
812 the boundary layer and the lower free troposphere, *Atmos. Chem. Phys.*, 13, 11059–11071, [https://doi.org/10.5194/acp-13-](https://doi.org/10.5194/acp-13-11059-2013)
813 11059-2013, 2013.
- 814 Zahn, A., Weppner, J., Widmann, H., Schlote-Holubek, K., Burger, B., Kühner, T., Franke, H.: A fast and precise
815 chemiluminescence ozone detector for eddy flux and airborne application, *Atmos. Meas. Tech.*, 5 (2), 363–375.
816 <https://doi.org/10.5194/amt-5-363-2012>, 2012.
- 817 Zarzana, K. J., Min, K.-E., Washenfelder, R. A., Kaiser, J., Krawiec-Thayer, M., Peischl, J., Neuman, J. A., Nowak, J. B.,
818 Wagner, N. L., Dubè, W. P., St. Clair, J. M., Wolfe, G. M., Hanisco, T. F., Keutsch, F. N., Ryerson, T. B., and Brown, S. S.:
819 Emissions of Glyoxal and Other Carbonyl Compounds from Agricultural Biomass Burning Plumes Sampled by Aircraft,
820 *Environ. Sci. Technol.*, 51, 11761–11770, <https://doi.org/10.1021/acs.est.7b03517>, 2017.
- 821 Ziereis, H., Minikin, A., Schlager, H., Gayet, J.F., Auriol, F., Stock, P., Baehr, J., Petzold, A., Schumann, U., Weinheimer, A.,
822 Ridley, B., and Ström, J.: Uptake of reactive nitrogen on cirrus cloud particles during INCA, *Geophys. Res. Lett.*, 31(5), 2004.